

A magnetic field study of two fast-rotating, radio bright M dwarfs

StKM 1-1262 and V374 Peg

S. Bellotti^{1,2}, P. I. Cristofari^{1,3}, J. R. Callingham^{4,5}, J. Morin⁶, P. Petit², A. A. Vidotto¹, M. Jardine⁷, L. Arnold⁸, R. D. Kavanagh^{5,4}, J. Llama⁹, and H. Vedantham^{4,10}

¹ Leiden Observatory, Leiden University, PO Box 9513, 2300 RA Leiden, The Netherlands
e-mail: bellotti@strw.leidenuniv.nl

² Institut de Recherche en Astrophysique et Planétologie, Université de Toulouse, CNRS, IRAP/UMR 5277, 14 avenue Edouard Belin, F-31400, Toulouse, France

³ Center for Astrophysics | Harvard & Smithsonian, 60 Garden Street, Cambridge, MA 02138, United States

⁴ ASTRON, Netherlands Institute for Radio Astronomy, Oude Hoogeveensedijk 4, Dwingeloo, 7991 PD, The Netherlands.

⁵ Anton Pannekoek Institute for Astronomy, University of Amsterdam, Science Park 904, 1098 XH, Amsterdam, The Netherlands

⁶ Laboratoire Univers et Particules de Montpellier, Université de Montpellier, CNRS, F-34095, Montpellier, France

⁷ School of Physics and Astronomy, University of St Andrews, North Haugh, St Andrews, Fife, Scotland, KY16 9SS

⁸ Canada-France-Hawaii Telescope, 65-1238 Mamalahoa Hwy, Kamuela, HI 96743, USA

⁹ Lowell Observatory, 1400 W. Mars Hill Rd. Flagstaff, AZ. 86001. USA

¹⁰ Kapteyn Astronomical Institute, University of Groningen, PO Box 800, 9700 AV Groningen, The Netherlands

Received ; accepted

ABSTRACT

Context. Radio observations at low frequencies are sensitive to the magnetic activity of stars and the plasma environment surrounding them, so one can scrutinize the conditions under which stellar space weather develops and impacts exoplanets. The accurate interpretation of the processes underlying the radio signatures requires a detailed characterisation of the stellar magnetism.

Aims. We study two M dwarfs, namely StKM 1-1262 (M0 type, $P_{\text{rot}} = 1.24$ d) and V374 Peg (M4 type, $P_{\text{rot}} = 0.4455$ d), which were detected recently with the LOW Frequency ARray (LOFAR). StKM 1-1262 exhibited the typical signature of a type-II radio burst, potentially resulting from a coronal mass ejection event. V374 Peg manifested low-frequency radio emission with high brightness temperature and low degree of polarisation, suggesting an electron-cyclotron maser instability emission mechanism. In this work, we provide recent observational constraints on the magnetic field of both stars.

Methods. We analysed spectropolarimetric observations of these M dwarfs collected with the SpectroPolarimètre InfraRouge (SPIRou). Firstly, we refined the stellar parameters such as effective temperature, surface gravity, and metallicity, and measured the average surface magnetic flux via modelling of Zeeman broadening in unpolarised spectra. We then applied Zeeman-Doppler imaging to least-squares deconvolution line profiles in circular polarisation to reconstruct their large-scale magnetic fields. We also reconstructed a brightness map for the two stars by means of Doppler imaging.

Results. StKM 1-1262 has a total, unsigned magnetic field of 3.53 ± 0.06 kG on average and the large-scale magnetic field topology is predominantly poloidal, dipolar and moderately axisymmetric, with an average strength of 300 G. V374 Peg has an unsigned magnetic field of 5.46 ± 0.09 kG and the large-scale field is poloidal, dipolar and axisymmetric, with an average strength of 800 G. For StKM 1-1262, we found a strong (Pearson $\rho = -0.96$) anti-correlation between the total magnetic field and the effective temperature which is reminiscent of the tight link between small-scale magnetic fields and surface inhomogeneities. For V374 Peg, we found a moderate ($\rho = -0.43$) anti-correlation, possibly due to a more even distribution of surface features.

Conclusions. The large-scale magnetic field topology of StKM 1-1262 is similar to other stars with similar fundamental parameters like mass and rotation period, and the brightness map features one dark spot which is responsible for the rotational modulation of the total magnetic field and the retrieved effective temperature. For V374 Peg, the magnetic topology and the brightness map are similar to previous reconstructions indicating a temporal stability of approximately 14-yr.

Key words. Stars: magnetic field – Stars: activity – Techniques: polarimetric

1. Introduction

A central goal of exoplanetology is to find Earth-like planets that potentially host life. According to the canonical definition, assessing the potential habitability of a planet requires knowledge about the distance (or insolation) of the planet from the star (Kasting et al. 1993; Kopparapu 2013). However, this is a first-order assessment, and additional details such as the stellar magnetic field (Driscoll & Bercovici 2013), the planetary volcanic and tectonic activity (Lenardic et al. 2016; Seales & Lenardic

2021), the distribution of oceans (Cockell et al. 2016), the asteroid impacts (Childs et al. 2022), and the binarity of the host star (Jaime et al. 2014; Cuntz 2015; Cuntz & Wang 2020) are needed to obtain a comprehensive definition of habitability. The space weather and radiation environment in which exoplanets orbit is also crucial in this context (Vidotto et al. 2013; Airapetian et al. 2017, 2020). For instance, X-ray and UV radiation can drive atmospheric escape and alter its chemical constituents, ultimately shaping the evolution of planetary atmospheres (Lammer et al.

2003; Penz & Micela 2008; Owen & Jackson 2012; Rugheimer et al. 2015; Carolan et al. 2019; Van Looveren et al. 2024).

Coronal mass ejections (CMEs) are expulsions of hot coronal plasma and magnetic field into the heliosphere with speeds ranging from 100 to 2000 km s⁻¹ (Nindos et al. 2008; Webb & Howard 2012). They represent a major constituent of the space weather in the Solar System and a continuous exposure is expected to lead to erosion of planetary atmospheres over time (Lammer et al. 2007; Khodachenko et al. 2007). Similar effects are anticipated on other stars (Lammer 2013; Cherenkov et al. 2017), but there has yet to be an unambiguous detection of an extrasolar CME, despite substantial observational effort (e.g. Crosley et al. 2016; Crosley & Osten 2018). The incidence and energetics of these phenomena are thus not constrained empirically, which prevents us from assessing the habitability of other systems in a comprehensive manner.

Radio observations of stellar systems allow one to investigate stellar magnetic activity and the space weather conditions of extrasolar planets (see Callingham et al. 2024, and references therein). Observing a type II radio burst represents a detection of plasma radial motion away from the star, because electrons are accelerated by shocks at the leading edges of outward-moving CMEs which generate the typical frequency sweep (Cane et al. 2002; Gopalswamy et al. 2008; Osten & Wolk 2017; Majumdar et al. 2021). A type II radio burst is thus a ‘smoking gun’ signature of CMEs, but it has been elusive for stars other than the Sun.

Another puzzle coming from radio observations of stellar systems concerns the low-frequency radio emission detected from both active and quiescent M dwarfs within the LOFAR Two-meter Sky Survey (LoTSS Shimwell et al. 2017, 2022). Specifically, these observations unravelled a population of M1–M6 dwarfs manifesting highly circularly polarised ($\geq 60\%$), high brightness temperature ($> 10^{12}$ K), coherent, low-frequency (on the order of MHz) radio emission (Callingham et al. 2021). To explain these findings, there are two main categories of processes: plasma emission or electron-cyclotron maser instability (ECMI) emission. The former occurs when flares and CMEs inject hot plasma into colder plasma (Dulk et al. 1985; Matthews 2019) and is correlated with stellar magnetic activity (McLean et al. 2012; Villadsen & Hallinan 2019; Callingham et al. 2021). The M dwarfs detected within the LoTSS survey span various activity levels, suggesting that the radio emission may not be only activity-driven which finds support from analyses of flare activity conducted with the Transiting Exoplanet Survey Satellite (TESS; Ricker et al. 2015) as shown by Pope et al. (2021).

For ECMI-driven emission (Wu & Lee 1979; Treumann 2006), the scenario sees an acceleration of electrons towards the star, powering auroral processes similar to Jupiter (Zarka 1998). A first possibility is that, at a certain distance from the star, the stellar magnetic field cannot impose co-rotation of the surrounding plasma. This breakdown of co-rotation generates a lag between the plasma disk and the star’s magnetosphere, and ultimately a current system that accelerates electrons towards the star (Nichols et al. 2012; Pineda et al. 2017; Marques et al. 2017). A second possibility translates the Jupiter interaction with its moon Io into a star-planet one, for which a planet orbits within the Alfvén surface of the host star and perturbs or reconnects with the stellar magnetic field, driving electron acceleration (Lazio et al. 2004; Zarka 2007; Turnpenney et al. 2018; Vidotto et al. 2019; Vedantham et al. 2020). Although there are candidates for star-planet interactions, no exoplanet has been conclusively detected via low-frequency radio emission yet

(Lynch et al. 2018; Vedantham et al. 2020; Pope et al. 2021; Turner et al. 2021; Pérez-Torres et al. 2021).

Considering the sensitivity of radio observations to the plasma environment around a star, interpreting such observations requires an accurate model of the stellar magnetic environment and wind (e.g. Vidotto et al. 2014; Kavanagh et al. 2019, 2021, 2022; Alvarado-Gómez et al. 2022; Elekes & Saur 2023; Peña-Moñino et al. 2024). In turn, such model is dictated by our knowledge on the magnetic field of the star, whose large-scale configuration can be reconstructed from spectropolarimetric time series via Zeeman-Doppler imaging (ZDI) (Semel 1989; Donati & Brown 1997). Over the years, ZDI has been applied extensively, revealing a variety of field geometries for low-mass stars as well as their temporal evolution (e.g. Petit et al. 2005; Donati et al. 2008; Morin et al. 2008b, 2010; Hébrard et al. 2016; Kochukhov & Lavail 2017; Lavail et al. 2018; Folsom et al. 2018; Bellotti et al. 2023b, 2024).

Here, we analyse recent spectropolarimetric observations of two stars, StKM 1-1262 and V374 Peg, and characterise their large-scale magnetic field. These two stars were detected within the LoTSS survey (Tasse et al. 2021; Yiu et al. 2024). StKM 1-1262 is an early M dwarf for which a candidate type-II radio burst was detected as an isolated event, with the characteristic frequency sweep of a typical solar type-II burst but more than four orders of magnitude radio luminous (Callingham et al. 2025). The constraint of the large-scale magnetic field geometry in the current work is used to determine whether a CME could have sufficient kinetic energy to escape the large-scale field and could drive a super-Alfvénic shock (Callingham et al. 2025). V374 Peg is an active, fully convective mid-M dwarf known to exhibit frequent flares (Korhonen et al. 2010; Vida et al. 2016), a strong (~ 1 kG), poloidal, and axisymmetric large-scale magnetic field (Morin et al. 2008a), and a powerful wind (Vidotto et al. 2011). Radio emission from V374 Peg was detected with the Very Large Array in a frequency band of 4–8 GHz (Hallinan et al. 2009), and the modulation of the radio light curve due to stellar rotation was fit by Llama et al. (2018) using an ECMI-driven model. Additional radio observations were obtained within the LoTSS survey (120–168 MHz) in 2018 and more recently in 2024, bracketing our spectropolarimetric observations. The reconstructed large-scale magnetic field in this work will then be used as boundary condition to simulate the stellar environment of V374 Peg and better understand which ECMI mechanism is powering the observed low-frequency radio emission in a follow-up study.

This paper is structured as follows. In Sect. 2 we describe the spectropolarimetric data set. In Sect. 3 we outline the modelling of Zeeman broadening and intensification of unpolarised spectra to measure the total, unsigned magnetic field intensity. In Sect. 4 and Sect. 5, we describe the analysis of circular polarisation spectra to measure the longitudinal magnetic field and to reconstruct the large-scale magnetic field geometry by means of ZDI, respectively. We then show the reconstruction of the brightness maps of StKM 1-1262 and V374 Peg with Doppler imaging in Sect. 6 and finally draw our conclusions in Sect. 7.

2. Observations

The observations analysed in this work were obtained in circular polarisation mode with the SpectroPolarimètre InfraRouge (SPIRou) (Donati et al. 2020), the stabilised high-resolution near-infrared spectropolarimeter mounted on the 3.6 m Canada–France–Hawaii Telescope (CFHT) atop Mauna Kea, Hawaii. SPIRou operates between 0.96 and 2.5 μ m

Table 1. Properties of StKM 1-1262 and V374 Peg.

Name	StKM 1-1262	V374 Peg
Spectral Type	M0V	M4V
H [mag]	8.15 ^a	7.04 ^a
Distance [pc]	40.9 ^b	9.1 ^b
T_{eff} [K]	$3933 \pm 31^{\dagger}$	$3228 \pm 30^{\dagger}$
$\log g$ [cgs]	$4.65 \pm 0.05^{\dagger}$	$4.72 \pm 0.05^{\dagger}$
M/H [dex]	$-0.07 \pm 0.10^{\dagger}$	$0.07 \pm 0.10^{\dagger}$
Mass [M_{\odot}]	0.64 ^c	0.30 ^c
Radius [R_{\odot}]	0.63 ^c	0.31 ^c
P_{rot} [d]	1.24 ^d	0.4455 ^e
$v_{\text{eq}} \sin i$ [km s ⁻¹]	$25.04 \pm 0.10^{\dagger}$	$36.73 \pm 0.17^{\dagger}$
i [°]	$> 70^{\dagger}$	70 ^e

Notes. The listed properties are: identifier, spectral type, H band magnitude, distance, effective temperature, surface gravity, metallicity, stellar mass, stellar radius, rotation period, equatorial projected velocity, and inclination used in ZDI. The parameters marked with \dagger are derived in this work. The references are: *a*) Cutri et al. (2003), *b*) Gaia Collaboration (2020), *c*) Kervella et al. (2022), *d*) Colman et al. (2024), and *e*) Morin et al. (2008a).

(*YJHK* bands) at a spectral resolving power of $R \sim 70\,000$. Optimal extraction of spectra in unpolarised (Stokes I) and circularly polarised (Stokes V) light was carried out with *A PipelinE to Reduce Observations* (APERO), a fully automatic reduction package installed at CFHT (Cook et al. 2022). The observations of both stars were reduced with APERO v0.7.288. The journal of the observations is given in Table A.1 and Table A.2.

StKM 1-1262 was observed for 17 nights between January and March 2024, spanning a period of 41 days. We recorded a S/N at 1650 nm per spectral element between 210 and 278, with a mean of 246. Two observations (23 and 28 February) did not reach enough S/N to produce meaningful Stokes V LSD profiles (see Sect. 4), so they were discarded. V374 Peg was observed 55 times between August 14th and 23th in 2021. The recorded S/N oscillated between 86 and 189, with an average of 162. In Table 1, we provide the fundamental stellar parameters derived and used in this work for both stars.

The observations of the StKM 1-1262 and V374 Peg are phased according to the ephemeris

$$\text{HJD} = \text{HJD}_0 + P_{\text{rot}} \cdot n_{\text{cyc}}. \quad (1)$$

In the formula, HJD_0 is the reference heliocentric Julian date (2460330.1563 for StKM 1-1262, and 2459440.7902 for V374 Peg), P_{rot} is the stellar rotation period (see Table 1), and n_{cyc} is the number of rotation cycles.

3. Total magnetic field and atmospheric characterisation

We estimated the average small-scale magnetic field strength at the stellar surface of StKM 1-1262 and V374 Peg following the approach described in Cristofari et al. (2023a,b). Our process relies on synthetic spectra computed from MARCS model atmospheres (Gustafsson et al. 2008) with ZeeTurbo (Cristofari et al. 2023a), a tool built from the Turbospectrum (Plez 2012) and Zeeman (Landstreet 1988; Wade et al. 2001; Folsom et al. 2016) codes. Specifically, we computed a grid of synthetic spectra for different set of atmospheric parameters, with T_{eff} ranging from 3200 to 4400 K, $\log g$ ranging from 4.0

to 5.0 dex in steps of 0.5 dex, and [M/H] ranging from -0.75 to 0.75 dex in steps of 0.25 dex. The chosen ranges are wide enough to encompass typical parameters for M dwarfs and act as uniform priors. For each set of atmospheric parameters, we computed spectra with different magnetic field intensities, ranging from 0 to 10 kG in steps of 2 kG, assuming that the magnetic field is radial in all points of the photosphere.

A model of the observed spectrum is obtained with a linear combination of the spectra computed for the different magnetic fields intensities so that $S = \sum_i f_i S_i$, with S the model spectrum, S_i the spectrum computed for a i kG field, and f_i the associated filling factor. We rely on an MCMC process to derive the set of atmospheric parameters, filling factors, and projected rotational velocity ($v_{\text{eq}} \sin i$) leading the best fit to the data and estimate formal error bars (see also Cristofari et al. 2023a,b, for more details). Our method is inherently sensitive to systematics which are not fully reflected by our formal error bars. Following Cristofari et al. (2022), we inflate the error bars by quadratically adding 30 K, 0.05 dex, and 0.10 dex to T_{eff} , $\log g$, and [M/H], respectively.

For both stars, we begin by applying our process to template spectra obtained by taking the median of all available spectra. For StKM 1-1262, our process yields $T_{\text{eff}} = 3933 \pm 31$ K, $\log g = 4.65 \pm 0.05$ dex, [M/H] = -0.07 ± 0.10 dex and $v_{\text{eq}} \sin i = 25.04 \pm 0.10$ km s⁻¹. For V374 Peg, our analysis yields $T_{\text{eff}} = 3228 \pm 30$ K, $\log g = 4.72 \pm 0.05$ dex, [M/H] = 0.07 ± 0.10 dex and $v_{\text{eq}} \sin i = 36.73 \pm 0.17$ km s⁻¹. Our atmospheric estimates are reported in Table 1.

For StKM 1-1262, our best fit on the template spectrum yields an average small-scale magnetic field of $\langle B_I \rangle = 3.53 \pm 0.06$ kG, with most of the magnetic intensity distributed on the 2 and 4 kG components ($\sim 87\%$ of the total magnetic flux, see Fig. 1). The value $\langle B_I \rangle = 3.53$ kG is consistent with that obtained for fast-rotating, early M dwarfs like OT Ser ($\langle B_I \rangle = 3.2$ kG; Shulyak et al. 2019) and YY Gem ($\langle B_I \rangle = 3.2 - 3.4$ kG; Kochukhov & Shulyak 2019). For V374 Peg, our process yields an average small-scale magnetic field of $\langle B_I \rangle = 5.46 \pm 0.09$ kG. The distribution of filling factors shows more contribution from the higher components, with the 4, 6 and 8 kG components accounting for 90 % of the total magnetic flux. In contrast to StKM 1-1262, the 2 kG component only amount to 4 % of the magnetic flux of V374 Peg (see Fig. 1).

For each star, we repeat our process, this time analysing each individual spectrum, and fixing the values of $\log g$ and [M/H] to those listed in Table 1. This approach allows us to simultaneously explore the temporal variations of $\langle B_I \rangle$ and temperature. Figure 2 shows $\langle B_I \rangle$ computed for each observation of StKM 1-1262 and V374 Peg, colour-coded with the associated value of T_{eff} .

For StKM 1-1262, the $\langle B_I \rangle$ range from ~ 4.50 to ~ 3.25 kG, and exhibit an evident modulation at the stellar rotation period of 1.24 d. We note a clear anti-correlation between $\langle B_I \rangle$ and T_{eff} (Pearson correlation coefficient $\rho = -0.96$). Specifically, we observe $\langle B_I \rangle$ to be highest around phase 0.0, when the retrieved T_{eff} is lowest. Such behaviour was already captured for the active M dwarfs AU Mic (Artigau et al. 2024), EV Lac, and DS Leo (Cristofari et al. 2025). As we will describe from Doppler imaging in Sect. 6, such behaviour tracks the presence of a starspot or a group of starspots, which are cooler than the quiet photosphere.

We further use the anti-correlation between $\langle B_I \rangle$ and temperature to estimate the spot coverage of StKM 1-1262. We fit a line $\langle B_I \rangle$ as a function of temperature, yielding a slope of -54 ± 5 K kG⁻¹ and an intercept of 4139 ± 18 K (see also Fig. B.1). We attribute the intercept of this fit to the temper-

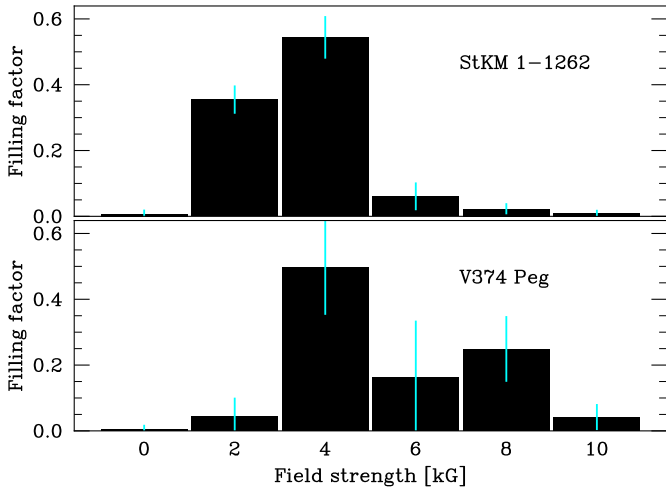


Fig. 1. Distribution of the magnetic flux on the different magnetic components. The top panel refers to StKM 1-1262 and the bottom panel to V374 Peg.

ature of the quiet photosphere (T_{\max}). Following the relation of Berdyugina (2005), we derive a spot temperature for StKM 1-1262 of $T_{\text{spot}} = 3303 \pm 14$ K. Given a temperature $T = 3933$ K (see also Table 1), we then compute the fraction of stellar surface occupied by spots, f , such that

$$f = \frac{T_{\max} - T}{T_{\max} - T_{\text{spot}}}.$$
 (2)

Injecting the effective temperature obtained for StKM 1-1262 into equation 2, we derived a spot coverage of about $f = 25\%$.

For V374 Peg, no clear rotational modulation of $\langle B_l \rangle$ is observed, which can be attributed to lower S/N of individual spectra rendering the fitting procedure more challenging. We find a moderate anti-correlation (Pearson correlation coefficient $\rho = -0.43$) between our temperature and $\langle B_l \rangle$ measurements, with a linear fit yielding a slope of -37 ± 7 K kG $^{-1}$ and an intercept of 3461 ± 43 K. Relying on the relation of Berdyugina (2005), we derive a spot temperature $T_{\text{spot}} = 2979 \pm 15$, and deduce a spot coverage of about 48%.

4. Longitudinal magnetic field

We computed mean line profiles using least-squares deconvolution (LSD; Donati et al. 1997; Kochukhov et al. 2010) and in particular the Python LSDpy package (Folsom et al. 2025).¹ Both the Stokes I and V spectra are deconvolved with a line list, to obtain individual, high-signal-to-noise ratio (S/N) profiles summarising the properties of hundreds of spectral lines. The line list contains absorption lines in the stellar spectrum and with the associated line features such as depth, and sensitivity to Zeeman effect (commonly known as the Landé factor g_{eff}). For our stars, we used a synthetic line list corresponding to a local thermodynamic equilibrium model (Gustafsson et al. 2008) characterised by $\log g = 5.0$ [cm s $^{-2}$], $v_{\text{micro}} = 1$ km s $^{-1}$, and $T_{\text{eff}} = 3500$ K. The adopted line list contains 1400 atomic photospheric lines between 950–2600 nm with depth larger than 3% the continuum level. The masks were synthesised using the Vienna Atomic Line Database² (VALD, Ryabchikova et al. 2015). We set the LSD

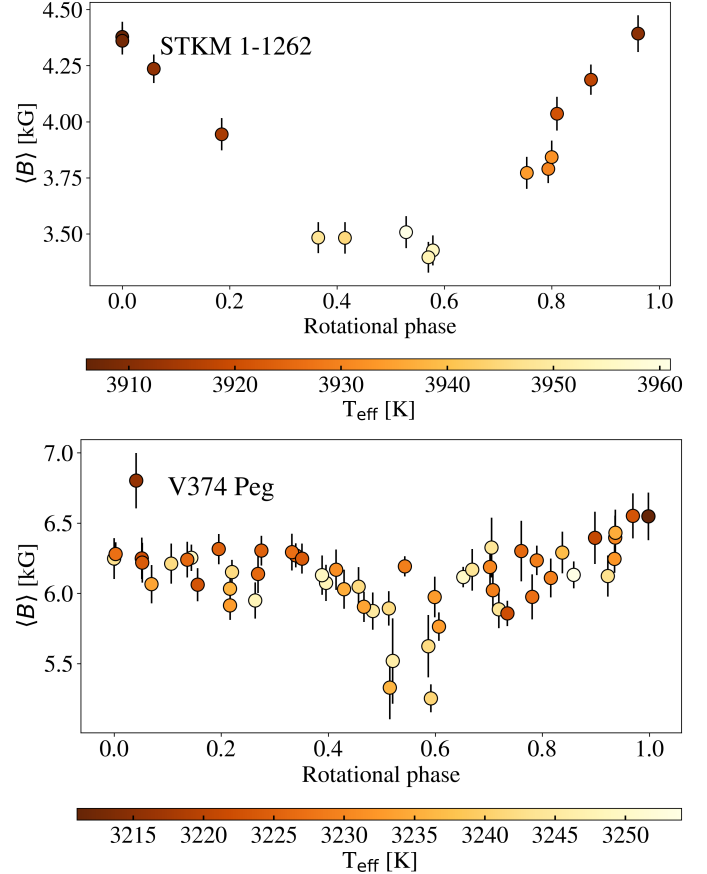


Fig. 2. Total magnetic field measurements of StKM 1-1262 and V374 Peg as a function of rotational phase. The data points are colour-coded with the effective temperature obtained from spectral modelling (see Sect. 3). The rotational phases are computed according to Eq. 1, using the stellar rotation period listed in Table 1.

normalisation wavelength and g_{eff} to 1700 nm and 1.2, respectively.

We computed the disk-integrated, line-of-sight projected component of the large-scale magnetic field following Donati et al. (1997). We used the general formula as in Cotton et al. (2019),

$$B_{\ell} = \frac{h}{\mu_B \lambda_0 g_{\text{eff}}} \frac{\int v V(v) dv}{\int (I_c - I(v)) dv},$$
 (3)

where λ_0 and g_{eff} are the normalisation wavelength and Landé factor of the LSD profiles, V is the LSD Stokes profile in circular polarisation, I is the LSD Stokes profile in unpolarised light, I_c is the continuum level, v is the radial velocity associated to a point in the spectral line profile in the star's rest frame, h is the Planck's constant and μ_B is the Bohr magneton. To express it as in Rees & Semel (1979) and Donati et al. (1997), one can use $hc/\mu_B = 0.0214$ Tm, where c is the speed of light in m s $^{-1}$.

For StKM 1-1262, the computation of B_{ℓ} was carried out within ± 55 km s $^{-1}$ from line centre at -3.9 km s $^{-1}$ for both Stokes I and V LSD profiles. As shown in Fig. 3, the values range between -127 and -8 G, with a median value of -74 G and a median error bar of 12 G. The error bars are estimated from formal propagation of Eq. 3. The phase-folded B_{ℓ} time series does not feature an evident modulation at the stellar rotation period, but rather higher frequency variations around the first harmonic of P_{rot} . When the B_{ℓ} data points are colour-coded based on T_{eff} in

¹ The code is available at <https://github.com/folsomcp/LSDpy>

² <http://vald.astro.uu.se/> using the Montpellier mirror to request locally MARCS model atmospheres.

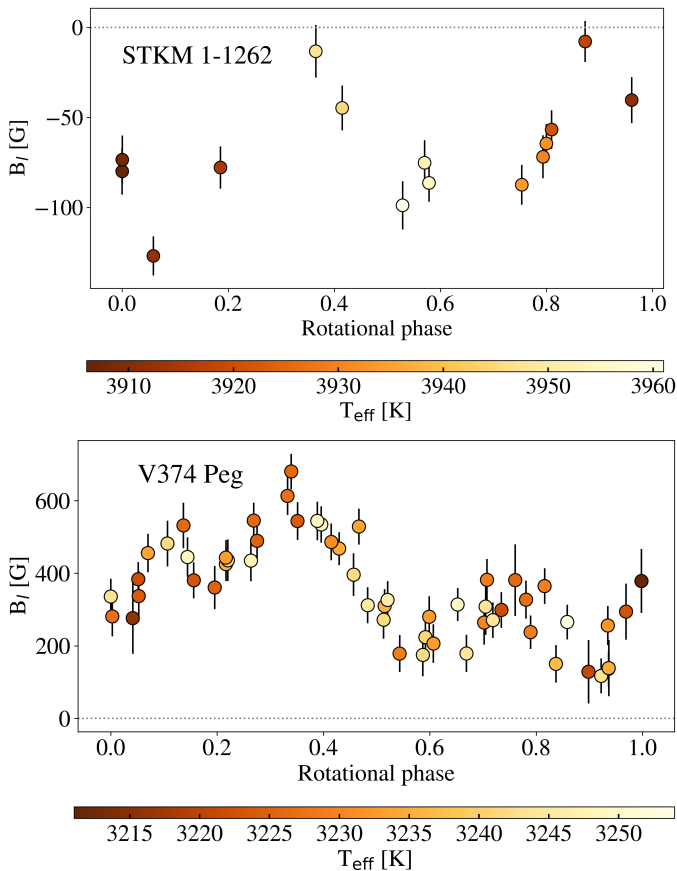


Fig. 3. Longitudinal magnetic field measurements of StKM 1-1262 and V374 Peg. The panels show B_ℓ as a function of rotational phase for StKM 1-1262 and V374 Peg. The rotational phases are computed according to Eq. 1, using the rotational period listed in Table 1.

a similar manner as in Fig. 2, we do not observe a correlation (Pearson $\rho = 0.01$, see also Fig. B.1).

For V374 Peg, we set an integration range of $\pm 80 \text{ km s}^{-1}$ from line centre at -3.0 km s^{-1} , and we found values between 117 and 680 G, with a median of 330 G and a median error bar of 50 G (see Fig. 3). The modulation of the B_ℓ time series sees an increase around phase 0.3 and a decrease around phase 0.8, but the values are always positive. This can indicate a tilted dipolar configuration of the large-scale field, as it will be explained in Sect. 5. When colour-coded by T_{eff} , the B_ℓ data points do not reveal any evident correlation (Pearson $\rho = -0.08$), as also shown in Fig. B.1.

Our range of B_ℓ measurements are consistent with previous ESPaDOnS observations performed by Morin et al. (2008a), as shown in Fig. 4. Their observations in August 2005, August 2006, and September 2009 resulted in average B_ℓ values of 338 G, 309 G, and 307 G. Combined with our observations, we do not see significant variations in the mean and range of B_ℓ values, potentially suggesting that the large-scale magnetic field has remained stable.

5. Magnetic field topology

The characterisation of the large-scale magnetic field of StKM 1-1262 and V374 Peg was performed with Zeeman-Doppler imaging (Semel 1989; Donati & Brown 1997). The algorithm compares observed and model Stokes V LSD profiles iteratively, fitting the spherical harmonics coefficients $\alpha_{\ell,m}$, $\beta_{\ell,m}$, and $\gamma_{\ell,m}$ (with

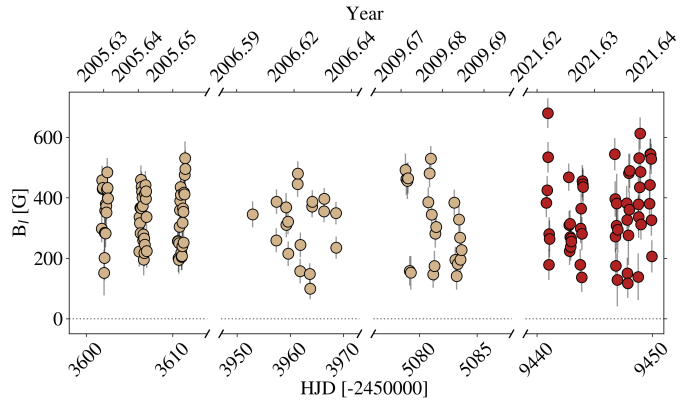


Fig. 4. Long-term measurements of V374 Peg's longitudinal magnetic field. The leftmost epochs (coloured with light brown) represent the August 2005, August 2006, and September 2009 time series analysed by Morin et al. (2008a). The rightmost (dark brown) time series corresponds to the data analysed in this work.

ℓ and m the degree and order of the mode, respectively), until they match within a target reduced χ^2 . Because the inversion problem is ill-posed, a maximum-entropy regularisation scheme is applied to obtain the field map compatible with the data and with the lowest information content (for more details see Skilling & Bryan 1984; Donati & Brown 1997). The magnetic field vector is modelled as the sum of a poloidal and a toroidal component, which are both expressed with spherical harmonics formalism (Lehmann & Donati 2022). We used the python implementation zdipy with the inclusion of the Unno-Rachkovsky's solutions to polarised radiative transfer equations (see Folsom et al. 2018; Bellotti et al. 2024) and the filling factor formalism of Morin et al. (2008b).

The parameters of the Unno-Rachkovsky models (see e.g. del Toro Iniesta 2003; Landi Degl'Innocenti & Landolfi 2004) are the Gaussian width (w_G), the Lorentzian width (w_L), the ratio of the line to continuum absorption coefficients (η_0), and the slope of the source function in the Milne-Eddington atmosphere (β). More information on their implementation in the zdipy code can be found in Erba et al. (2024) and Bellotti et al. (2024). We performed a χ^2 minimisation between synthetic and observed Stokes I profiles for a grid of parameters, in order to find the set of parameters that best represents our observations. For StKM 1-1262, we found $w_G = 9.4 \text{ km s}^{-1}$, $w_L = 8.0 \text{ km s}^{-1}$, and $\eta_0 = 13.0$, and for V374 Peg, we found $w_G = 9.0 \text{ km s}^{-1}$, $w_L = 10.0 \text{ km s}^{-1}$, and $\eta_0 = 12.2$. The value of β is fixed to 0.25 (for more details, see Erba et al. 2024; Bellotti et al. 2024). The filling factors f_I and f_V represent the fraction of the cell of the stellar surface grid covered by magnetic regions and magnetic regions producing net circular polarisation, respectively (Morin et al. 2008b; Kochukhov 2021). We attempted to constrain such parameters with a χ^2 minimisation but the results were inconclusive, so we fixed both filling factors to 1.0 for both stars.

5.1. Stellar input parameters

The ZDI reconstruction requires physical and geometrical parameters of the star such as: inclination, projected equatorial velocity $v_{\text{eq}} \sin i$, rotation period, differential rotation rate, limb darkening coefficient and maximum degree of spherical harmonics decomposition (ℓ_{max}). The linear limb darkening coefficient was fixed to 0.2, the value corresponding H band observations (Claret & Bloemen 2011).

For $v_{\text{eq}} \sin i$, we set the values obtained from the spectral fitting procedure (see Sect. 3), namely 25.04 km s^{-1} for StKM1 1-1262 and 36.73 km s^{-1} for V374 Peg. The value of $v_{\text{eq}} \sin i$ determines the attainable spatial resolution encapsulated in ℓ_{max} (e.g. Morin et al. 2008a). We conservatively set ℓ_{max} to 10 for the two stars, since most of the magnetic energy is stored in the $\ell \leq 7$ modes.

We attempted a differential rotation search for both stars as described in Petit et al. (2002) but the results were inconclusive, so we assumed solid body rotation. The rotation period of StKM 1-1262 was estimated to be $1.240 \pm 0.003 \text{ d}$ from TESS photometry (Colman et al. 2024), and for V374 Peg we adopted a value of 0.4455 d (see Morin et al. 2008a). All these values are summarised in Table 1.

Finally, the inclination of the star is estimated comparing the stellar radius available in the literature with the value obtained geometrically from rotation period and $v_{\text{eq}} \sin i$. Formally, $R \sin i = P_{\text{rot}} v_{\text{eq}} \sin i / 50.59$ where the denominator accounts for the unit conversion of the variables involved (P_{rot} in d, $v_{\text{eq}} \sin(i)$ in km s^{-1} , and R in R_{\odot}). For StKM 1-1262, we found $R \sin i = 0.633 \pm 0.006 R_{\odot}$ while Kervella et al. (2022) reported $R = 0.630 R_{\odot}$, indicating that the viewing angle of the star is likely equator-on (i.e. 90°). As input for ZDI, we assumed 70° to prevent mirroring effects between the north and south hemispheres of the star. For V374 Peg we adopted a value of 70° consistently with Morin et al. (2008a).

5.2. Reconstruction

The Stokes V profiles of StKM 1-1262 and their ZDI models are shown in Fig. C.1 and the ZDI map is shown in Fig. 5. We fitted the observed Stokes V LSD profiles down to $\chi_r^2 = 1.0$. As reported in Table 2, the large-scale magnetic geometry is predominantly poloidal, with a strong dipolar component accounting for 75% of the poloidal magnetic energy and also a significant (20%) quadrupolar component. The toroidal field is also substantial, containing 13% of the magnetic energy. The magnetic field is tilted, with only 47% of the total energy stored in the axisymmetric modes (that is, $m = 0$). This mainly follows the fact that the poloidal component is non-axisymmetric (41%), whereas the toroidal component is axisymmetric (82%). The average magnetic field strength is 300 G.

The Stokes V profiles of V374 Peg are shown in Fig. C.3 and the ZDI map is shown in Fig. 5. We fitted the observed Stokes V LSD profiles to a χ_r^2 of 1.0. The large-scale magnetic geometry is predominantly poloidal (99%), dipolar (97%), and axisymmetric (92%). The average magnetic field strength is 780 G (see Table 2).

6. Doppler imaging

Using the time series of Stokes I LSD profiles, we applied Doppler imaging to reconstruct a brightness image of the surface of StKM 1-1262 and of V374 Peg. The principle of the technique is based on the distortions that surface inhomogeneities induce on the shape of spectral lines. Owing to the Doppler effect, there is a correlation between the location of the spectral distortion on the profile and the location of the inhomogeneity on the stellar surface. The occurrence of a distortion at a certain time yields information on the longitude of the surface inhomogeneity, while the extent of the distortion across the profile informs one of the latitude of the spot. Therefore, by monitoring the temporal mod-

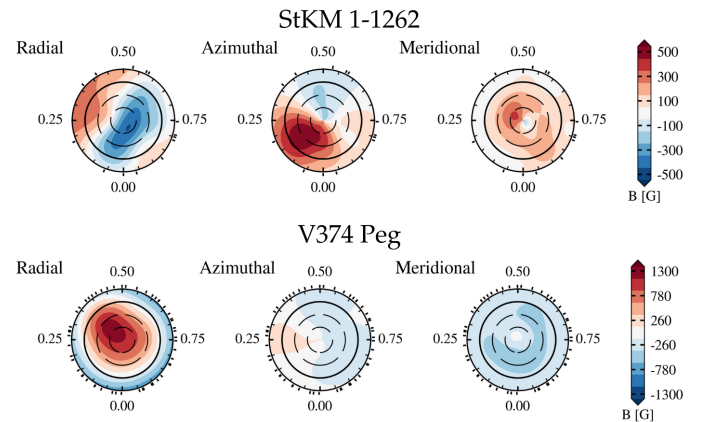


Fig. 5. Reconstructed large-scale magnetic field maps in flattened polar view. StKM 1-1262 is shown in the top row and V374 Peg in the bottom row. From the left, the radial, azimuthal, and meridional components of the magnetic field vector are illustrated. Concentric circles represent different stellar latitudes: -30° , $+30^\circ$, and $+60^\circ$ (dashed lines), as well as the equator (solid line). The radial ticks are located at the rotational phases when the observations were collected. The rotational phases are computed with Eq. 1 using the first observation of each individual epoch (see Table A.1). The colour bar indicates the polarity and strength (in G) of the magnetic field.

ulation of such distortions one can retrieve a 2D brightness map (Deutsch 1957; Vogt & Penrod 1983; Rice et al. 1989).

The longitudinal resolution of the reconstructed map scales with $v_{\text{eq}} \sin i$ (e.g. Hussain et al. 2009; Morin et al. 2008a). Values of $v_{\text{eq}} \sin i \geq 15 - 20 \text{ km s}^{-1}$ typically ensure sufficient rotational broadening of the line profile and ultimately the reliability of the reconstructed map. The $v_{\text{eq}} \sin i$ of StKM 1-1262 and V374 Peg are suitable for such reconstruction (see Table 1). We used the Doppler imaging implementation provided in the `zdipy` code and the input parameters are those described in Sect. 5.

For StKM 1-1262, the Stokes I data set can be fitted to a S/N level of 2800. Fig. 6 shows the dynamic spectrum of StKM 1-1262 corresponding to the observations (leftmost panel), model (central panel), and residuals (rightmost panel). The observations panel exhibits the signatures of a mid latitude dark spot or cluster of spots travelling over the line profiles from the blue to the red wing and crossing the line of sight around phase 0.0 (green colour), as well as a bright feature crossing at phase 0.5 (brown colour). The tilt of these signatures is reasonably the same, indicating that the brightness inhomogeneities are located at similar latitudes. The signatures are well-reproduced in the model panel, since the residuals do not feature evident systematic or rotationally modulated structure.

The brightness map of StKM 1-1262 is shown in Fig. 7, in which we observe consistent features as in the dynamic spectrum. There is a dark spot or a cluster of smaller ones centred around phase 0.95. This feature is located at a latitude of approximately 60° and has a surface occupancy of 9%. The map also exhibits a bright feature at phase 0.5, which is roughly 20% more intense than the quiet photosphere. This is slightly larger than what reported for the Sun (Hirayama & Moriyama 1979). Overall, the observational cadence does not sample the longitudes of StKM 1-1262 densely and the attainable spatial resolution is limited by $v_{\text{eq}} \sin i$ for Doppler imaging, therefore we caution to not over-interpret the brightness map. When compared to the results of Zeeman broadening modelling, we observe a striking correlation between the reconstructed brightness features and the rotationally modulated total magnetic flux and effective tem-

Table 2. Properties of the magnetic maps.

Star	χ_r^2	$\langle B_V \rangle$ [G]	$ B_{\max} $ [G]	$\langle B^2 \rangle$ $\times 10^5$ G 2	f_{pol} [%]	f_{tor} [%]	f_{dip} [%]	f_{quad} [%]	f_{oct} [%]	f_{axi} [%]	$f_{\text{axi, pol}}$ [%]	$f_{\text{axi, tor}}$ [%]
StKM 1-1262	1.00	300	646	1.08	86.2	13.8	74.6	20.0	4.3	46.8	41.1	82.1
V374 Peg	1.00	783	1396	7.03	99.0	1.0	96.8	2.4	0.8	92.2	92.2	92.4

Notes. The following quantities are listed: star's name, target χ_r^2 of the ZDI reconstruction, mean unsigned magnetic strength, maximum unsigned magnetic strength, total reconstructed magnetic energy, poloidal and toroidal magnetic energies as a fraction of the total energy, dipolar, quadrupolar, and octupolar magnetic energy as a fraction of the poloidal energy, axisymmetric magnetic energy as a fraction of the total energy, poloidal axisymmetric energy as a fraction of the poloidal energy, toroidal axisymmetric energy as a fraction of the toroidal energy.

perature derived from spectral line modelling (see Sect. 3 and Fig. 2). Specifically, we observe the presence of a dark spot or a cluster of small ones at phase 0.0, which is where the total magnetic flux is highest and the effective temperature is smallest. In Appendix C, we describe the simultaneous modelling of Stokes I and V LSD profiles.

For V374 Peg, the Stokes I data set can be fitted to a S/N level of 2700. The dynamic spectra shown in Fig. 6 exhibit similarities with those of Morin et al. (2008a), with multiple brightness inhomogeneities crossing the line of sight. Signatures of dark spots are present around phases 0.0 and 0.4, and bright features at phases 0.2, 0.5, and 0.7. The rotationally modulated distortions travelling across the Stokes I profile are well-reproduced by the model, albeit a systematic discrepancy visible especially in the right part of the residuals (the red wing part of the line profile) as vertical bands. As already noted by Morin et al. (2008a), this discrepancy does not affect the imaging process.

Our reconstructed brightness map of V374 Peg is illustrated in Fig. 7 and it is consistent with the dynamic spectra. We note two dark regions around latitudes 50–60° with roughly 20% less intensity than the quiet photosphere, and three bright regions at similar latitudes with up to 40% larger intensity. While it is not possible to compare this Doppler map with those of Morin et al. (2008a) exactly, because our model accounts for both dark and bright regions, there is an overall agreement in terms of multitude of inhomogeneities and complexity of the surface on V374 Peg. The fact that the brightness maps of V374 Peg are consistent, despite being about 14 yr apart, is also consistent with the analysis of photometric light curves of Vida et al. (2016) which suggests a spot configuration that is stable over about 16 yr. In the case of V374 Peg, the comparison between the brightness map and the time series of total magnetic flux and effective temperature is less straightforward than StKM 1-1262, due to the lack of a clear rotational modulation of $\langle B_I \rangle$ and T_{eff} .

7. Discussion and conclusions

We have analysed SPIRou spectropolarimetric time series observations in circular polarisation mode of two stars, StKM 1-1262 and V374 Peg. Our aim is to provide robust and updated constraints on the magnetic field of the two stars, which is a fundamental ingredient to understand the mechanisms driving their detected radio emission. For StKM 1-1262, the detected radio emission has identical frequency and polarisation properties as fundamental plasma emission from a Solar Type II burst, likely representing one of the few evidences of an extrasolar type-II burst (Tasse et al. 2021; Callingham et al. 2025). Such detection suggests that the CMEs can occur for stars whose field is substantially stronger than the Sun's (Alvarado-Gómez et al. 2018; Strickert et al. 2024). The magnetic field characterisation

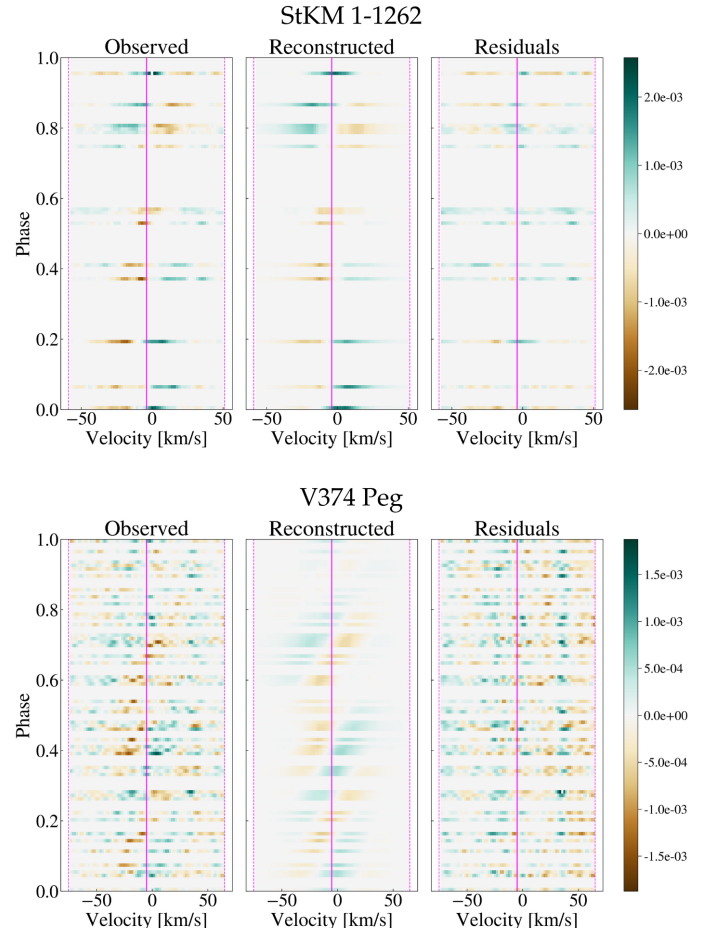
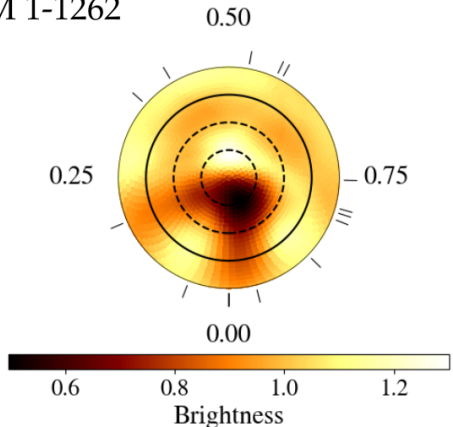


Fig. 6. Dynamic spectra of StKM 1-1262 and V374 Peg. The Stokes I profiles are phase-folded according to Eq. 1 and stacked vertically. From left, the panels show the observed, reconstructed and residual profiles. The colour bar indicates the flux values of Stokes I LSD profiles. In the observed and reconstructed panels, the Stokes I are median subtracted, hence positive and negative values of the colour bar indicate dark and bright features, respectively. The median subtraction removes stationary bumps, making them more evident in the residuals panel. The vertical solid line locates the radial velocity of the stars (-3.9 km s $^{-1}$ for StKM 1-1262 and -5.0 km s $^{-1}$ for V374 Peg) and the two dashed lines are located at the extremes of the intervals for the computation of B_{ℓ} and ZDI (see Sect. 4 and Sect. 5).

of StKM 1-1262 performed in this work has been used in Callingham et al. (2025) to support such conclusion.

From the unpolarised spectra, we modelled Zeeman broadening and intensification, constraining the total unsigned magnetic field $\langle B_I \rangle$ to be 3.53 ± 0.06 kG for StKM 1-1262 and 5.46 ± 0.09 kG for V374 Peg. In terms of mass and rotation period,

StKM 1-1262



V374 Peg

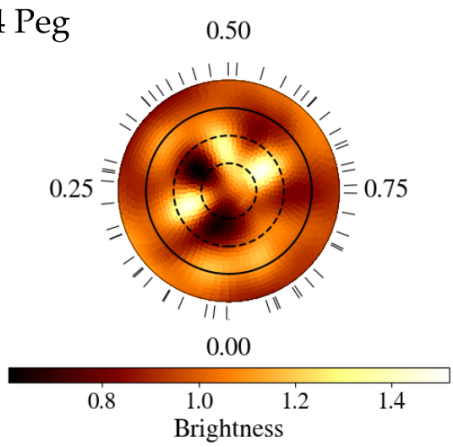


Fig. 7. Reconstructed brightness maps of StKM 1-1262 and V374 Peg. The colour bar indicates the brightness relative to the quiet photosphere, which is equal to 1.0.

StKM 1-1262 falls close to the binary system YY Gem, whose magnetic field characterisation was carried out by Kochukhov & Shulyak (2019). The authors measured a total magnetic field of 3.2–3.4 kG for the two stars in the binary, which is compatible with our value for StKM 1-1262. Our results are also similar to the early-M dwarf OT Ser, with a total unsigned magnetic field of 3.2 kG (Shulyak et al. 2019). For V374 Peg, our measurement is compatible with the estimate of 4.4 ± 1.0 kG by Shulyak et al. (2019) within uncertainties, and it is also consistent with stars in the vicinity of V374 Peg in terms of mass and rotation period such as EQ Peg B (4.2 ± 1.0 kG; Shulyak et al. 2017).

We used the spectral fitting procedure to derive values of surface temperature T_{eff} and $\langle B_I \rangle$ simultaneously. We found a strong anti-correlation between total magnetic flux and effective temperature for StKM 1-1262, which is in agreement with the tight connection between the stellar surface temperature variations and the small-scale magnetic field, as already pointed out in Artigau et al. (2024) and Cristofari et al. (2025). For V374 Peg, we only obtained a moderate anti-correlation, which is most likely due to a combination of factors such as the low S/N of the observations, the larger $v_{\text{eq}} \sin(i)$ (hence rotational broadening), the low contrast between spots and quiet photosphere (of about 300 K), and potentially a more dense and homogeneous distribution of surface features as opposed to StKM 1-1262. The combined action of several surface spots distributed homogeneously could also explain the lack of a clear rotational modulation of T_{eff} and $\langle B_I \rangle$ for V374 Peg. This would be consistent

with the fact that V374 Peg falls in the supersaturated regime of the activity-rotation relation (Wright et al. 2011), for which coronal X-ray emission decreases below the saturation level of $L_X/L_{\text{bol}} \sim 10^{-3}$ with increasing rotation (e.g. Prosser et al. 1996). In fact, although V374 Peg is expected to be more active than StKM 1-1262, its X-ray emission is $L_X = 2.75 \times 10^{28}$ erg/s (Delfosse et al. 1998), which is about one order of magnitude lower than that of StKM 1-1262 ($L_X = 2.20 \times 10^{29}$ erg/s Agüeros et al. 2009). In this scenario, V374 Peg’s surface would be completely covered with active regions in contrast to StKM 1-1262.

From the circularly polarised spectra, we first measured the longitudinal field. We found an average of -67 G for StKM 1-1262 and 351 G for V374 Peg, consistently showing a difference in magnetic activity level between the two stars. We then reconstructed the large-scale magnetic field by means of Zeeman-Doppler imaging, and the results are contextualised in Fig. 8. We obtained predominantly poloidal-dipolar configurations with moderate axisymmetry for StKM 1-1262 and high axisymmetry for V374 Peg. The average magnetic field is 300 G and 800 G for the two stars. The ratio $\langle |B_V| \rangle / \langle B_I \rangle$ between the magnetic field strength as recovered by circularly polarised (that is, ZDI) and unpolarised (that is, Zeeman broadening modelling) light is 8.5% for StKM 1-1262 and 15% for V374 Peg. Values of up to 10% are typical for partly-convective M dwarfs (Reiners & Basri 2009; Morin et al. 2010; Kochukhov 2021), and up to 20% for fully convective M dwarfs depending on the large-scale field geometry (see e.g. Kochukhov 2021). Both our findings are therefore within expectations.

Our ZDI reconstruction of StKM 1-1262 is in overall agreement with stars of similar properties like YY Gem (Kochukhov & Shulyak 2019). The situation is similar for V374 Peg, since Morin et al. (2008a) also reconstructed a largely poloidal-dipolar field with high degree of axisymmetry. This suggests that the large-scale magnetic field of V374 Peg is stable over time, but the wide observational gap of approximately 10 yr observations prevent us from being conclusive. Additional observations conducted on a yearly basis will provide a definitive answer.

We also reconstructed the brightness map of both stars. For StKM 1-1262, we found the surface to be characterised by a dark spot lying approximately at rotational phase 0.0 (see Fig. 7). The structure of the brightness map is corroborated by the time series of $\langle B_I \rangle$ and T_{eff} , since their rotational modulation correlates with the presence of such starspot. For V374 Peg, we reconstructed a more complex map, with multiple dark and bright regions, which is in overall agreement with previous reconstructions (Morin et al. 2008a) and the view that this star has a more homogeneous spot distribution. In this case, we did not observe a clear rotational modulation of $\langle B_I \rangle$ or T_{eff} , hence connecting them to the Doppler map is less straightforward. From our analysis of the $\langle B_I \rangle$ - T_{eff} anti-correlation, we obtained spot coverages of 25% and 48% for StKM 1-1262 and V374 Peg, which are higher than the mean spot coverage reconstructed via Doppler imaging of 9% and 17% , respectively. Such discrepancy could stem from the fact that the temperature variations studied in Sect. 3 may be the result of large spots as well as several small ones, making the empirical relation in Eq. 2 more sensitive to different spatial scales than Doppler imaging. In fact, the spatial resolution attainable by Doppler imaging, which is further deteriorated by S/N considerations, is mostly limited to big spots or small spots clustered together.

Finally, the LoTTS survey has detected several low-mass stars with radio observations, regardless of the magnetic activity level of the star (Callingham et al. 2021). Shedding more light on the physical mechanism driving the radio emission, whether

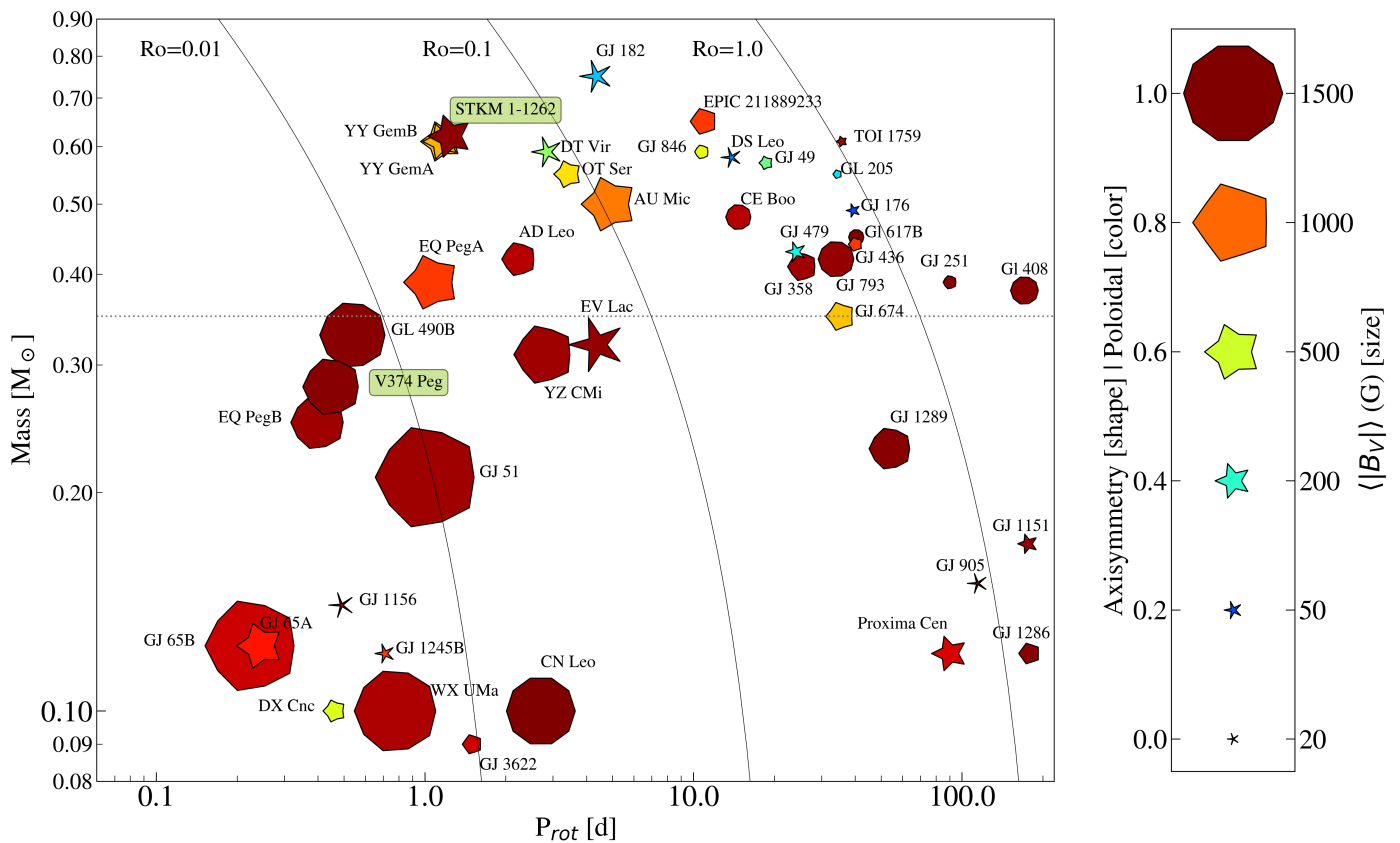


Fig. 8. Properties of the magnetic topologies for cool, main-sequence stars obtained via Zeeman-Doppler Imaging. The locations of StKM 1-1262 and V374 Peg are highlighted. The y- and x-axes represent the mass and rotation period of the star. Gray curves illustrate different Rossby numbers ($Ro = 0.01, 0.1$ and 1.0) and are obtained using the empirical relations of Wright et al. (2018). The Rossby number is the ratio between the rotation period of a star and the convective turnover time. The symbol size, colour and shape encodes the ZDI average field strength, poloidal/toroidal energy fraction and axisymmetry (see Petit et al. 2008; Morgenthaler et al. 2012; Fares et al. 2013; Boro Saikia et al. 2015; do Nascimento et al. 2016; Boro Saikia et al. 2016; Hussain et al. 2016; Alvarado-Gómez et al. 2015; Folsom et al. 2016, 2018; Kochukhov & Shulyak 2019; Folsom et al. 2020; Klein et al. 2021; Willamo et al. 2022; Martioli et al. 2022; Bellotti et al. 2023a; Lehmann et al. 2024, for the data used). For stars with multiple reconstructions, the data represent the most recent ZDI maps.

planet- or plasma-induced for instance, requires a robust constraint on the magnetic field. Therefore, spectropolarimetric observations of these low-mass stars are required to fully understand their magnetism and plasma environment.

Acknowledgements. We would like to thank Prof. B. Pope for the contribution to the SPIRou observing proposal of StKM 1-1262 and the comments for this manuscript. This publication is part of the project "Exo-space weather and contemporaneous signatures of star-planet interactions" (with project number OCENW.M.22.215 of the research programme "Open Competition Domain Science- M"), which is financed by the Dutch Research Council (NWO). PC and AAV acknowledge funding from the European Research Council (ERC) under the European Union's Horizon 2020 research and innovation programme (grant agreement No 817540, ASTROFLOW). JRC acknowledges funding from the European Union via the European Research Council (ERC) grant Ephaus (project number 101166008) AAV acknowledges funding from the Dutch Research Council (NWO), with project number VI.C.232.041 of the Talent Programme Vici. MMJ acknowledges support from STFC consolidated grant number ST/R000824/1. Based on observations obtained at the Canada-France-Hawaii Telescope (CFHT) which is operated by the National Research Council of Canada, the Institut National des Sciences de l'Univers of the Centre National de la Recherche Scientifique of France, and the University of Hawaii. This work has made use of the VALD database, operated at Uppsala University, the Institute of Astronomy RAS in Moscow, and the University of Vienna; Astropy, 12 a community-developed core Python package for Astronomy (Astropy Collaboration et al. 2013, 2018); NumPy (van der Walt et al. 2011); Matplotlib: Visualization with Python (Hunter 2007); SciPy (Virtanen et al. 2020) and PyAstronomy (Czesla et al. 2019).

References

Agüeros, M. A., Anderson, S. F., Covey, K. R., et al. 2009, ApJS, 181, 444
 Airapetian, V. S., Barnes, R., Cohen, O., et al. 2020, International Journal of Astrobiology, 19, 136
 Airapetian, V. S., Glocer, A., Khazanov, G. V., et al. 2017, ApJ, 836, L3
 Alvarado-Gómez, J. D., Cohen, O., Drake, J. J., et al. 2022, ApJ, 928, 147
 Alvarado-Gómez, J. D., Drake, J. J., Cohen, O., Moschou, S. P., & Garraffo, C. 2018, ApJ, 862, 93
 Alvarado-Gómez, J. D., Hussain, G. A. J., Grunhut, J., et al. 2015, A&A, 582, A38
 Artigau, É., Cadieux, C., Cook, N. J., et al. 2024, AJ, 168, 252
 Astropy Collaboration, Price-Whelan, A. M., Sipőcz, B. M., et al. 2018, AJ, 156, 123
 Astropy Collaboration, Robitaille, T. P., Tollerud, E. J., et al. 2013, A&A, 558, A33
 Bellotti, S., Fares, R., Vidotto, A. A., et al. 2023a, A&A, 676, A139
 Bellotti, S., Morin, J., Lehmann, L. T., et al. 2023b, A&A, 676, A56
 Bellotti, S., Morin, J., Lehmann, L. T., et al. 2024, A&A, 686, A66
 Berdyugina, S. V. 2005, Living Reviews in Solar Physics, 2, 8
 Boro Saikia, S., Jeffers, S. V., Morin, J., et al. 2016, A&A, 594, A29
 Boro Saikia, S., Jeffers, S. V., Petit, P., et al. 2015, A&A, 573, A17
 Callingham, J. R., Pope, B. J. S., Kavanagh, R. D., et al. 2024, Nature Astronomy, 8, 1359
 Callingham, J. R., Tasse, C., & Keers, R. 2025, Nature, accepted
 Callingham, J. R., Vedantham, H. K., Shimwell, T. W., et al. 2021, Nature Astronomy, 5, 1233
 Cane, H. V., Erickson, W. C., & Prestage, N. P. 2002, Journal of Geophysical Research (Space Physics), 107, 1315
 Carolan, S., Vidotto, A. A., Loesch, C., & Coogan, P. 2019, MNRAS, 489, 5784
 Cherenkov, A., Bisikalo, D., Fossati, L., & Möstl, C. 2017, ApJ, 846, 31
 Childs, A. C., Martin, R. G., & Livio, M. 2022, ApJ, 937, L41

Claret, A. & Bloemen, S. 2011, A&A, 529, A75

Cockell, C. S., Bush, T., Bryce, C., et al. 2016, Astrobiology, 16, 89

Colman, I. L., Angus, R., David, T., et al. 2024, AJ, 167, 189

Cook, N. J., Artigau, É., Doyon, R., et al. 2022, PASP, 134, 114509

Cotton, D. V., Evensberget, D., Marsden, S. C., et al. 2019, MNRAS, 483, 1574

Cristofari, P. I., Donati, J.-F., Bellotti, S., et al. 2025, A&A, 702, A111

Cristofari, P. I., Donati, J.-F., Folsom, C. P., et al. 2023a, MNRAS, 522, 1342

Cristofari, P. I., Donati, J. F., Masseron, T., et al. 2022, MNRAS, 511, 1893

Cristofari, P. I., Donati, J. F., Moutou, C., et al. 2023b, MNRAS, 526, 5648

Crosley, M. K. & Osten, R. A. 2018, ApJ, 862, 113

Crosley, M. K., Osten, R. A., Broderick, J. W., et al. 2016, ApJ, 830, 24

Cuntz, M. 2015, ApJ, 798, 101

Cuntz, M. & Wang, Z. 2020, Astronomische Nachrichten, 341, 402

Cutri, R. M., Skrutskie, M. F., van Dyk, S., et al. 2003, VizieR Online Data Catalog, II/246

Czesla, S., Schröter, S., Schneider, C. P., et al. 2019, PyA: Python astronomy-related packages

del Toro Iniesta, J. C. 2003, Introduction to Spectropolarimetry

Delfosse, X., Forveille, T., Perrier, C., & Mayor, M. 1998, A&A, 331, 581

Deutsch, A. J. 1957, AJ, 62, 139

do Nascimento, J. D., J., Vidotto, A. A., Petit, P., et al. 2016, ApJ, 820, L15

Donati, J. F. & Brown, S. F. 1997, A&A, 326, 1135

Donati, J. F., Cristofari, P. I., Finocci, B., et al. 2023, MNRAS, 525, 455

Donati, J.-F., Cristofari, P. I., Klein, B., Finocci, B., & Moutou, C. 2025, A&A, 700, A122

Donati, J. F., Kouach, D., Moutou, C., et al. 2020, MNRAS, 498, 5684

Donati, J. F., Morin, J., Petit, P., et al. 2008, MNRAS, 390, 545

Donati, J. F., Semel, M., Carter, B. D., Rees, D. E., & Collier Cameron, A. 1997, MNRAS, 291, 658

Driscoll, P. & Bercovici, D. 2013, Icarus, 226, 1447

Dulk, G. A., Steinberg, J. L., Lecacheux, A., Hoang, S., & MacDowall, R. J. 1985, A&A, 150, L28

Elekes, F. & Saur, J. 2023, A&A, 671, A133

Erba, C., Folsom, C. P., David-Uraz, A., et al. 2024, ApJ, 977, 84

Fares, R., Moutou, C., Donati, J. F., et al. 2013, MNRAS, 435, 1451

Folsom, C. P., Bouvier, J., Petit, P., et al. 2018, MNRAS, 474, 4956

Folsom, C. P., Erba, C., Petit, V., et al. 2025, Journal of Open Source Software, 10, 7891

Folsom, C. P., Ó Fionnagáin, D., Fossati, L., et al. 2020, A&A, 633, A48

Folsom, C. P., Petit, P., Bouvier, J., et al. 2016, MNRAS, 457, 580

Gaia Collaboration. 2020, VizieR Online Data Catalog: Gaia EDR3 (Gaia Collaboration, 2020), VizieR On-line Data Catalog: I/350. Originally published in: 2021A&A...649A...1G; doi:10.5270/esa-1ug

Gopalswamy, N., Yashiro, S., Akiyama, S., et al. 2008, Annales Geophysicae, 26, 3033

Gustafsson, B., Edvardsson, B., Eriksson, K., et al. 2008, A&A, 486, 951

Hallinan, G., Doyle, G., Antonova, A., et al. 2009, in American Institute of Physics Conference Series, Vol. 1094, 15th Cambridge Workshop on Cool Stars, Stellar Systems, and the Sun, ed. E. Stempels (AIP), 146–151

Hébrard, É. M., Donati, J. F., Delfosse, X., et al. 2016, MNRAS, 461, 1465

Hirayama, T. & Moriyama, F. 1979, Sol. Phys., 63, 251

Hunter, J. D. 2007, Computing in Science and Engineering, 9, 90

Hussain, G. A. J., Alvarado-Gómez, J. D., Grunhut, J., et al. 2016, A&A, 585, A77

Hussain, G. A. J., Collier Cameron, A., Jardine, M. M., et al. 2009, MNRAS, 398, 189

Jaime, L. G., Aguilar, L., & Pichardo, B. 2014, MNRAS, 443, 260

Kasting, J. F., Whitmire, D. P., & Reynolds, R. T. 1993, Icarus, 101, 108

Kavanagh, R. D., Vidotto, A. A., Klein, B., et al. 2021, MNRAS, 504, 1511

Kavanagh, R. D., Vidotto, A. A., Ó Fionnagáin, D., et al. 2019, MNRAS, 485, 4529

Kavanagh, R. D., Vidotto, A. A., Vedantham, H. K., et al. 2022, MNRAS, 514, 675

Kervella, P., Arenou, F., & Thévenin, F. 2022, A&A, 657, A7

Khodachenko, M. L., Ribas, I., Lammer, H., et al. 2007, Astrobiology, 7, 167

Klein, B., Donati, J.-F., Moutou, C., et al. 2021, MNRAS, 502, 188

Kochukhov, O. 2021, A&A, 29, 1

Kochukhov, O. & Lavalail, A. 2017, ApJL, 835, L4

Kochukhov, O., Makaganiuk, V., & Piskunov, N. 2010, A&A, 524, A5

Kochukhov, O. & Shulyak, D. 2019, ApJ, 873, 69

Kopparapu, R. K. 2013, ApJL, 767, L8

Korhonen, H., Vida, K., Husarik, M., et al. 2010, Astronomische Nachrichten, 331, 772

Lammer, H. 2013, Origin and Evolution of Planetary Atmospheres

Lammer, H., Lichtenegger, H. I. M., Kulikov, Y. N., et al. 2007, Astrobiology, 7, 185

Lammer, H., Selsis, F., Ribas, I., et al. 2003, ApJL, 598, L121

Landi Degl'Innocenti, E. & Landolfi, M. 2004, Polarization in Spectral Lines, Vol. 307

Landstreet, J. D. 1988, ApJ, 326, 967

Lavail, A., Kochukhov, O., & Wade, G. A. 2018, MNRAS, 479, 4836

Lazio, T., Joseph, W., Farrell, W. M., Dietrick, J., et al. 2004, ApJ, 612, 511

Lehmann, L. T. & Donati, J. F. 2022, MNRAS, 514, 2333

Lehmann, L. T., Donati, J. F., Fouqué, P., et al. 2024, MNRAS, 527, 4330

Lenardic, A., Jellinek, A. M., Foley, B., O'Neill, C., & Moore, W. B. 2016, Journal of Geophysical Research (Planets), 121, 1831

Llama, J., Jardine, M. M., Wood, K., Hallinan, G., & Morin, J. 2018, ApJ, 854, 7

Lynch, C. R., Murphy, T., Lenc, E., & Kaplan, D. L. 2018, MNRAS, 478, 1763

Majumdar, S., Patel, R., Pant, V., & Banerjee, D. 2021, ApJ, 919, 115

Marques, M. S., Zarka, P., Echer, E., et al. 2017, A&A, 604, A17

Martioli, E., Hébrard, G., Fouqué, P., et al. 2022, A&A, 660, A86

Matthews, L. D. 2019, PASP, 131, 016001

McLean, M., Berger, E., & Reiners, A. 2012, ApJ, 746, 23

Morgenthaler, A., Petit, P., Saar, S., et al. 2012, A&A, 540, A138

Morin, J., Donati, J. F., Forveille, T., et al. 2008a, MNRAS, 384, 77

Morin, J., Donati, J. F., Petit, P., et al. 2008b, MNRAS, 390, 567

Morin, J., Donati, J. F., Petit, P., et al. 2010, MNRAS, 407, 2269

Nichols, J. D., Burleigh, M. R., Casewell, S. L., et al. 2012, ApJ, 760, 59

Nindos, A., Aurass, H., Klein, K. L., & Trottet, G. 2008, Sol. Phys., 253, 3

Osten, R. A. & Wolk, S. J. 2017, in IAU Symposium, Vol. 328, Living Around Active Stars, ed. D. Nandy, A. Valio, & P. Petit, 243–251

Owen, J. E. & Jackson, A. P. 2012, MNRAS, 425, 2931

Peña-Moñino, L., Pérez-Torres, M., Varela, J., & Zarka, P. 2024, A&A, 688, A138

Penz, T. & Micela, G. 2008, A&A, 479, 579

Pérez-Torres, M., Gómez, J. F., Ortiz, J. L., et al. 2021, A&A, 645, A77

Petit, P., Dintrans, B., Solanki, S. K., et al. 2008, MNRAS, 388, 80

Petit, P., Donati, J. F., Aurière, M., et al. 2005, MNRAS, 361, 837

Petit, P., Donati, J. F., & Collier Cameron, A. 2002, MNRAS, 334, 374

Pineda, J. S., Hallinan, G., & Kao, M. M. 2017, ApJ, 846, 75

Plez, B. 2012, Turbospectrum: Code for spectral synthesis, Astrophysics Source Code Library, record ascl:1205.004

Pope, B. J. S., Callingham, J. R., Feinstein, A. D., et al. 2021, ApJ, 919, L10

Prosser, C. F., Randich, S., Stauffer, J. R., Schmitt, J. H. M. M., & Simon, T. 1996, AJ, 112, 1570

Rees, D. E. & Semel, M. D. 1979, A&A, 74, 1

Reiners, A. & Basri, G. 2009, A&A, 496, 787

Rice, J. B., Wehlau, W. H., & Khokhlova, V. L. 1989, A&A, 208, 179

Ricker, G. R., Winn, J. N., Vanderspek, R., et al. 2015, Journal of Astronomical Telescopes, Instruments, and Systems, 1, 014003

Rosén, L. & Kochukhov, O. 2012, A&A, 548, A8

Rugheimer, S., Kaltenegger, L., Segura, A., Linsky, J., & Mohanty, S. 2015, ApJ, 809, 57

Rybchikova, T., Piskunov, N., Kurucz, R. L., et al. 2015, Phys. Scr., 90, 054005

Seales, J. & Lenardic, A. 2021, arXiv e-prints, arXiv:2106.14852

Semel, M. 1989, A&A, 225, 456

Shimwell, T. W., Hardcastle, M. J., Tasse, C., et al. 2022, A&A, 659, A1

Shimwell, T. W., Röttgering, H. J. A., Best, P. N., et al. 2017, A&A, 598, A104

Shulyak, D., Reiners, A., Engeln, A., et al. 2017, Nature Astronomy, 1, 0184

Shulyak, D., Reiners, A., Nagel, E., et al. 2019, A&A, 626, A86

Skilling, J. & Bryan, R. K. 1984, MNRAS, 211, 111

Strickert, K. M., Evensberget, D., & Vidotto, A. A. 2024, MNRAS, 533, 1156

Tasse, C., Shimwell, T., Hardcastle, M. J., et al. 2021, A&A, 648, A1

Treumann, R. A. 2006, A&A Rev., 13, 229

Turner, J. D., Zarka, P., Grießmeier, J.-M., et al. 2021, A&A, 645, A59

Turnpenney, S., Nichols, J. D., Wynn, G. A., & Burleigh, M. R. 2018, ApJ, 854, 72

van der Walt, S., Colbert, S. C., & Varoquaux, G. 2011, Computing in Science and Engineering, 13, 22

Van Looveren, G., Güdel, M., Boro Saikia, S., & Kislyakova, K. 2024, A&A, 683, A153

Vedantham, H. K., Callingham, J. R., Shimwell, T. W., et al. 2020, Nature Astronomy, 4, 577

Vida, K., Kriskovics, L., Oláh, K., et al. 2016, A&A, 590, A11

Vidotto, A. A., Feeney, N., & Groh, J. H. 2019, MNRAS, 488, 633

Vidotto, A. A., Jardine, M., Morin, J., et al. 2013, A&A, 557, A67

Vidotto, A. A., Jardine, M., Morin, J., et al. 2014, MNRAS, 438, 1162

Vidotto, A. A., Jardine, M., Opher, M., Donati, J. F., & Gombosi, T. I. 2011, MNRAS, 412, 351

Villadsen, J. & Hallinan, G. 2019, ApJ, 871, 214

Virtanen, P., Gommers, R., Burovski, E., et al. 2020, scipy/scipy: SciPy 1.5.3

Vogt, S. S. & Penrod, G. D. 1983, PASP, 95, 565

Wade, G. A., Bagnulo, S., Kochukhov, O., et al. 2001, A&A, 374, 265

Webb, D. F. & Howard, T. A. 2012, Living Reviews in Solar Physics, 9, 3

Willamo, T., Lehtinen, J. J., Hackman, T., et al. 2022, A&A, 659, A71

Wright, N. J., Drake, J. J., Mamajek, E. E., & Henry, G. W. 2011, ApJ, 743, 48

Wright, N. J., Newton, E. R., Williams, P. K. G., Drake, J. J., & Yadav, R. K. 2018, MNRAS, 479, 2351

Wu, C. S. & Lee, L. C. 1979, ApJ, 230, 621

Yiu, T. W. H., Vedantham, H. K., Callingham, J. R., & Günther, M. N. 2024, A&A, 684, A3

Zarka, P. 1998, Journal of Geophysical Research, 103, 20159

Zarka, P. 2007, Planetary and Space Science, 55, 598

Appendix A: Journal of observations

In this appendix, we report the log of the observations for StKM 1-1262 and V374 Peg. The table includes the $\langle B_I \rangle$, T_{eff} , and longitudinal field measurements for the two stars.

Table A.1. List of observations for StKM 1-1262.

Date	UT [hh:mm:ss]	HJD [-2460330.1563]	n_{cyc} [s]	t_{exp}	S/N	σ_{LSD} [$10^{-5} I_c$]	B_{ℓ} [G]	$\langle B_I \rangle$ [kG]	T_{eff} [K]
January 20	15:45:04.50	0.0000	0.00	4x523	254	8.7	-80.0 ± 12.9	4.38 ± 0.07	3906 ± 4
January 21	15:50:58.02	1.0041	0.81	4x523	271	7.2	-56.8 ± 10.7	4.04 ± 0.08	3921 ± 4
January 23	15:36:47.78	2.9943	2.41	4x523	244	9.3	-44.8 ± 12.4	3.48 ± 0.07	3945 ± 3
January 30	15:34:46.05	9.9928	8.06	4x523	271	7.4	-127.0 ± 10.9	4.24 ± 0.06	3912 ± 3
February 15	12:55:56.27	25.8825	20.87	4x523	254	7.6	-7.9 ± 11.5	4.19 ± 0.07	3918 ± 3
February 17	14:12:10.61	27.9355	22.53	4x523	229	9.7	-98.9 ± 13.4	3.51 ± 0.07	3961 ± 3
February 18	15:05:37.19	28.9726	23.37	4x523	216	11.3	-13.3 ± 14.6	3.48 ± 0.07	3948 ± 4
February 19	15:30:16.00	29.9897	24.19	4x523	235	8.8	-77.9 ± 11.7	3.94 ± 0.07	3915 ± 3
February 20	15:45:20.56	31.0002	25.00	4x523	210	9.1	-73.6 ± 13.4	4.36 ± 0.06	3908 ± 3
February 21	14:10:33.49	31.9344	25.75	4x523	268	8.1	-87.5 ± 11.0	3.77 ± 0.07	3934 ± 3
February 22	14:43:39.96	32.9574	26.58	4x523	275	7.5	-86.4 ± 10.5	3.43 ± 0.07	3955 ± 3
February 25	13:37:16.21	35.9112	28.96	4x523	251	8.7	-40.4 ± 12.8	4.39 ± 0.08	3911 ± 3
February 26	14:24:21.07	36.9439	29.79	4x523	227	8.8	-71.9 ± 12.0	3.79 ± 0.06	3930 ± 3
February 27	13:31:08.50	37.9070	30.57	4x523	213	8.7	-75.2 ± 12.6	3.40 ± 0.07	3953 ± 3
March 02	13:37:56.10	41.9117	33.80	4x523	278	7.7	-64.5 ± 10.8	3.84 ± 0.07	3932 ± 3

Notes. The columns are: (1 and 2) date and universal time of the observations, (3) heliocentric Julian date, (4) rotational cycle of the observations found using Eq. 1, (5) exposure time of a polarimetric sequence, (6) signal-to-noise ratio at 1650 nm per polarimetric sequence, (7) RMS noise level of Stokes V signal in units of unpolarised continuum, (8) longitudinal magnetic field (see Eq 3) with error bar estimated from formal propagation, (9) average unsigned magnetic field, and (10) effective surface temperature.

Table A.2. List of observations for V374 Peg with the same format as Table A.1.

Date	UT [hh:mm:ss]	HJD [-2459440.7902]	n_{cyc} [s]	t_{exp}	S/N	σ_{LSD} [$10^{-5} I_c$]	B_{ℓ} [G]	$\langle B_I \rangle$ [kG]	T_{eff} [K]
August 14	06:57:49.49	0.0000	0.00	4x100	178	17.5	335.7 ± 49.2	6.25 ± 0.15	3243 ± 5
August 14	07:30:58.80	0.0230	0.05	4x100	186	18.0	383.5 ± 47.6	6.25 ± 0.15	3222 ± 4
August 14	09:16:44.06	0.0965	0.22	4x100	187	18.2	425.0 ± 46.7	6.03 ± 0.13	3236 ± 5
August 14	10:35:33.47	0.1512	0.34	4x100	178	18.3	680.3 ± 48.9	6.27 ± 0.09	3226 ± 4
August 14	11:11:49.73	0.1764	0.40	4x100	157	18.0	534.3 ± 50.4	6.07 ± 0.13	3248 ± 4
August 14	12:46:18.85	0.2420	0.54	4x100	163	16.3	178.5 ± 51.0	6.19 ± 0.07	3229 ± 4
August 14	13:22:01.20	0.2668	0.60	4x100	150	18.4	280.0 ± 56.3	5.97 ± 0.14	3233 ± 5
August 14	14:28:20.57	0.3129	0.70	4x100	146	20.9	264.0 ± 60.9	6.19 ± 0.17	3230 ± 5
August 16	06:19:28.34	1.9734	4.43	4x100	189	16.0	467.9 ± 45.3	6.03 ± 0.14	3235 ± 5
August 16	07:14:20.93	2.0115	4.52	4x100	184	17.0	309.5 ± 47.2	5.33 ± 0.23	3236 ± 4
August 16	08:03:33.62	2.0457	4.60	4x100	179	15.7	223.7 ± 45.9	5.25 ± 0.10	3241 ± 4
August 16	08:42:23.54	2.0726	4.66	4x100	187	16.2	313.8 ± 45.4	6.12 ± 0.07	3250 ± 4
August 16	09:25:00.04	2.1022	4.72	4x100	169	17.1	270.6 ± 48.8	5.89 ± 0.13	3244 ± 4
August 16	10:10:27.33	2.1338	4.79	4x100	175	16.1	237.6 ± 46.0	6.23 ± 0.10	3229 ± 4
August 16	10:54:42.21	2.1645	4.86	4x100	173	15.3	265.6 ± 47.8	6.13 ± 0.10	3254 ± 4
August 16	11:43:39.33	2.1985	4.94	4x100	162	17.3	255.8 ± 53.8	6.25 ± 0.10	3232 ± 4
August 17	06:16:08.47	2.9711	6.68	4x100	172	20.7	178.7 ± 51.2	6.17 ± 0.15	3244 ± 4
August 17	06:58:20.23	3.0004	6.74	4x100	167	18.0	298.8 ± 49.3	5.86 ± 0.09	3222 ± 5
August 17	07:50:23.44	3.0365	6.82	4x100	184	18.1	364.5 ± 49.4	6.11 ± 0.14	3229 ± 5
August 17	09:07:30.40	3.0901	6.94	4x100	177	17.5	136.7 ± 48.6	6.40 ± 0.16	3230 ± 4
August 17	09:50:16.61	3.1198	7.01	4x100	178	16.4	281.0 ± 54.8	6.28 ± 0.08	3227 ± 5
August 17	10:33:16.01	3.1496	7.08	4x100	169	16.7	455.6 ± 52.8	6.07 ± 0.14	3234 ± 4
August 17	11:20:59.43	3.1828	7.15	4x100	146	21.8	444.6 ± 54.4	6.25 ± 0.09	3249 ± 4
August 17	12:09:46.87	3.2166	7.23	4x100	150	18.9	435.5 ± 57.2	6.15 ± 0.09	3242 ± 5
August 20	06:06:45.26	5.9645	13.40	4x100	168	20.5	544.2 ± 53.3	6.13 ± 0.14	3249 ± 4
August 20	06:50:38.79	5.9950	13.47	4x100	155	18.0	395.9 ± 58.8	6.05 ± 0.14	3242 ± 5
August 20	07:26:51.78	6.0202	13.53	4x100	172	18.5	271.9 ± 52.2	5.89 ± 0.12	3242 ± 4
August 20	08:14:10.99	6.0530	13.60	4x100	161	18.7	174.8 ± 58.3	5.62 ± 0.22	3242 ± 5
August 20	09:29:52.77	6.1056	13.72	4x100	106	26.9	308.0 ± 77.8	6.33 ± 0.21	3244 ± 6

August 20	10:05:36.35	6.1304	13.78	4x100	118	31.8	380.9 \pm 98.8	6.30 \pm 0.21	3226 \pm 6
August 20	11:33:59.06	6.1918	13.91	4x100	128	30.2	128.4 \pm 87.4	6.39 \pm 0.19	3221 \pm 5
August 20	12:19:20.61	6.2233	13.98	4x100	124	26.6	294.2 \pm 77.4	6.55 \pm 0.16	3223 \pm 5
August 21	06:54:34.48	6.9977	15.73	4x100	150	19.4	381.7 \pm 57.5	6.02 \pm 0.15	3229 \pm 5
August 21	07:41:44.13	7.0305	15.80	4x100	173	19.1	327.1 \pm 52.5	5.97 \pm 0.16	3227 \pm 5
August 21	08:17:44.29	7.0555	15.86	4x100	178	18.6	150.1 \pm 51.6	6.29 \pm 0.15	3237 \pm 4
August 21	09:12:20.80	7.0934	15.94	4x100	186	16.6	117.0 \pm 48.2	6.12 \pm 0.15	3243 \pm 4
August 21	10:28:37.68	7.1464	16.06	4x100	86	30.9	276.2 \pm 98.5	6.80 \pm 0.20	3216 \pm 6
August 21	11:10:31.26	7.1755	16.12	4x100	154	23.3	481.9 \pm 63.2	6.21 \pm 0.14	3242 \pm 5
August 21	12:07:31.67	7.2151	16.21	4x100	145	23.8	360.6 \pm 59.4	6.32 \pm 0.11	3225 \pm 4
August 21	12:58:38.35	7.2506	16.29	4x100	167	19.1	489.2 \pm 57.0	6.30 \pm 0.11	3225 \pm 4
August 22	06:44:30.64	7.9908	17.96	4x100	121	27.0	138.5 \pm 77.6	6.43 \pm 0.16	3235 \pm 6
August 22	07:24:01.95	8.0182	18.02	4x100	123	30.7	378.4 \pm 88.2	6.55 \pm 0.17	3211 \pm 6
August 22	07:58:51.70	8.0424	18.07	4x100	132	22.2	337.0 \pm 69.6	6.22 \pm 0.14	3224 \pm 5
August 22	08:52:52.15	8.0799	18.16	4x100	156	20.8	531.6 \pm 62.6	6.24 \pm 0.13	3226 \pm 5
August 22	10:14:18.03	8.1364	18.28	4x100	159	19.1	434.7 \pm 56.9	5.95 \pm 0.13	3248 \pm 4
August 22	10:58:24.09	8.1671	18.35	4x100	162	16.7	613.0 \pm 52.6	6.29 \pm 0.13	3227 \pm 4
August 22	11:51:18.61	8.2038	18.44	4x100	173	17.2	486.0 \pm 50.6	6.17 \pm 0.14	3231 \pm 4
August 22	12:35:16.19	8.2343	18.50	4x100	173	17.6	311.7 \pm 49.7	5.87 \pm 0.13	3245 \pm 4
August 23	06:28:23.06	8.9796	20.18	4x100	176	18.6	380.5 \pm 49.8	6.06 \pm 0.12	3223 \pm 4
August 23	07:07:08.09	9.0065	20.24	4x100	182	17.9	442.9 \pm 49.0	5.91 \pm 0.10	3233 \pm 4
August 23	07:40:43.06	9.0298	20.29	4x100	182	17.8	545.0 \pm 49.3	6.14 \pm 0.13	3226 \pm 4
August 23	08:33:30.83	9.0665	20.37	4x100	180	17.8	543.8 \pm 52.0	6.25 \pm 0.11	3224 \pm 3
August 23	09:47:38.32	9.1179	20.49	4x100	184	18.8	528.6 \pm 49.7	5.90 \pm 0.11	3234 \pm 4
August 23	10:22:11.97	9.1419	20.54	4x100	166	21.6	326.3 \pm 51.8	5.52 \pm 0.30	3246 \pm 4
August 23	11:17:33.79	9.1804	20.63	4x100	155	17.3	206.2 \pm 53.4	5.76 \pm 0.10	3233 \pm 4

Appendix B: Additional figures

In this appendix, we provide additional figures related to the atmospheric characterisation of the two stars and the correlation analysis between the total unsigned magnetic field, the absolute value of the longitudinal magnetic field and the stellar surface temperature.

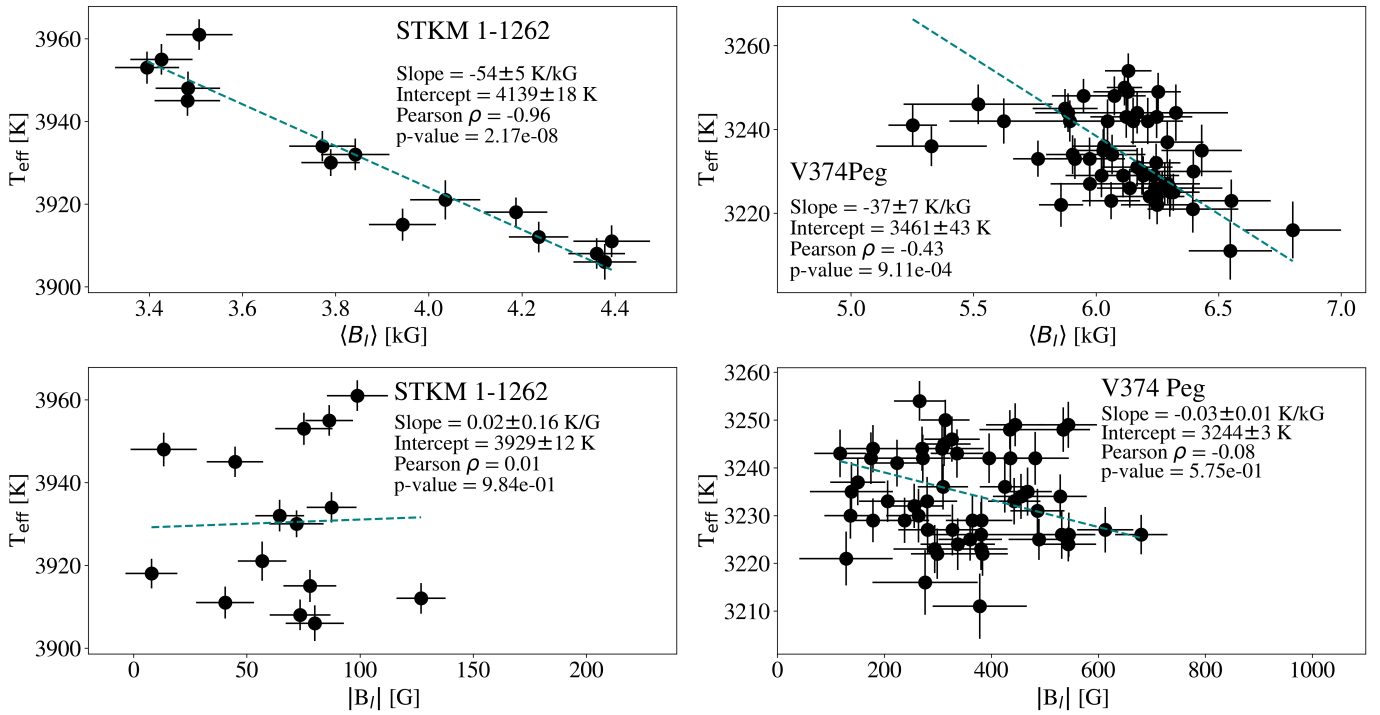


Fig. B.1. Correlation of the total unsigned field and longitudinal field with the stellar surface temperature. The left panels refer to STKM 1-1262 and the right ones to V374 Peg. The blue line indicates a linear fit, whose best-fit values are given in the each legend. We also include the Pearson correlation coefficient and the corresponding p-value.

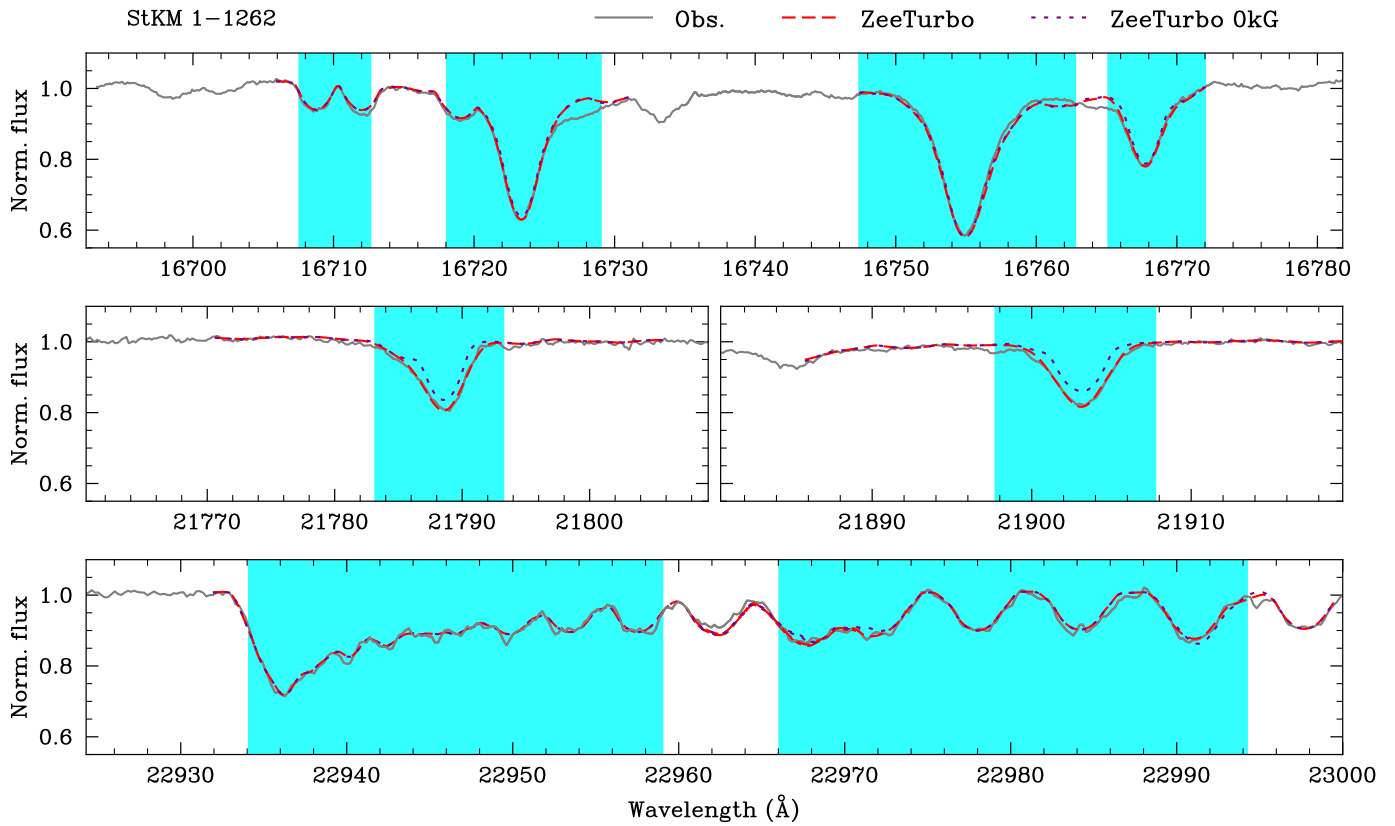


Fig. B.2. Example fit obtained on the template spectrum of StKM 1-1262. The cyan region shows regions on which the fit is performed.

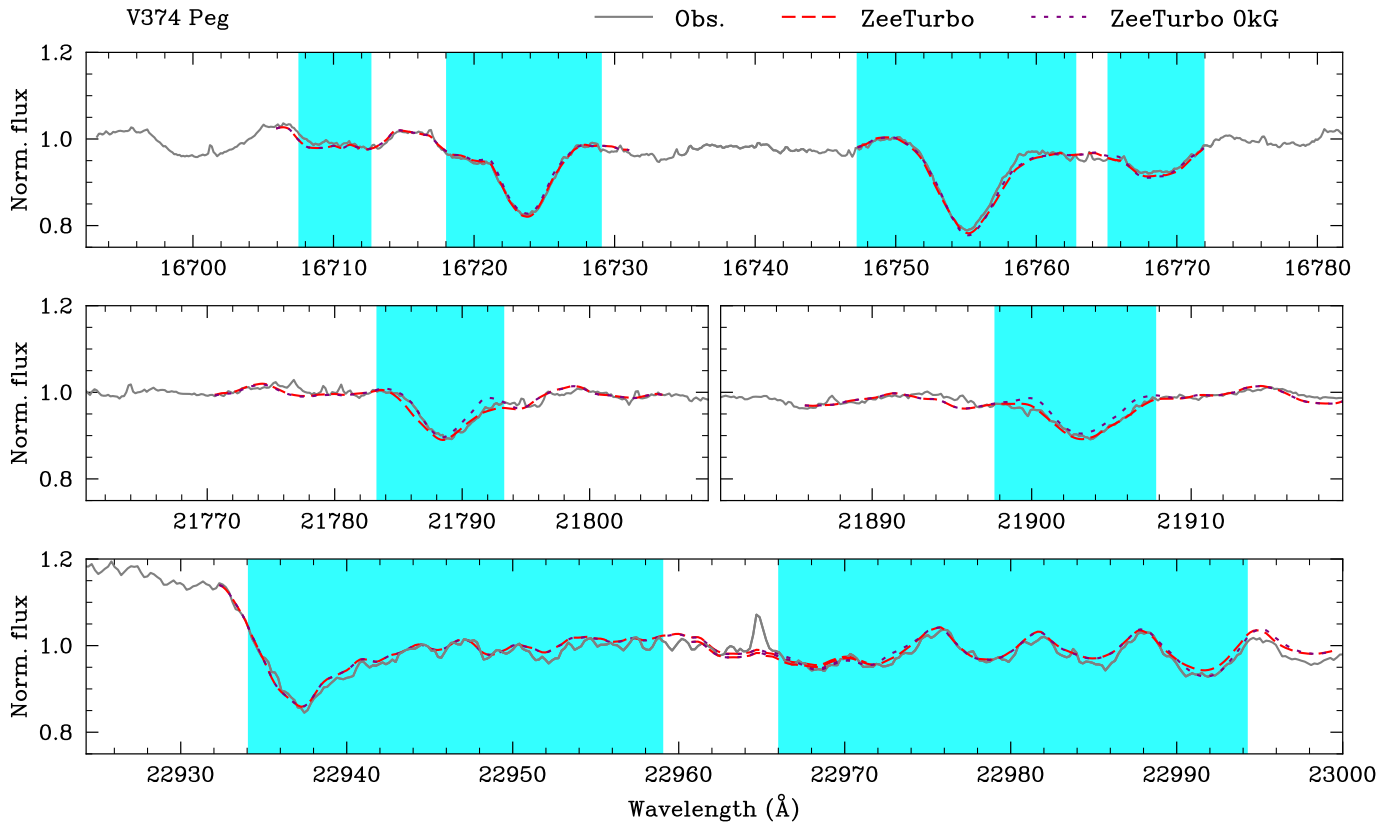


Fig. B.3. Same as Fig. B.2 for V374 Peg.

Appendix C: Simultaneous Stokes I and V modelling

In this appendix, we present the Stokes I and V models for both StKM 1-1262 and V374 Peg. In Fig. C.1 and Fig. C.3, we show the Stokes V LSD profiles associated to the magnetic maps presented in Sect. 5. In Fig. C.2 and Fig. C.4, we show the Stokes I LSD profiles associated to the brightness maps presented in Sect. 6.

When performing ZDI, one typical assumption is that the brightness of the photosphere is homogeneous. Rosén & Kochukhov (2012) tested the reliability of ZDI reconstructions when high-contrast temperature spots are modelled simultaneously to the magnetic geometry in ideal conditions (i.e. high S/N, dense phase coverage, and large $v_{\text{eq}} \sin i$). They found that the magnetic field strength is underestimated by 10-15% when temperature and magnetic spots are included, and by 30-60% when only magnetic spots are included. We decided to reconstruct the large-scale magnetic field of STKM 1-1262 and V374 Peg together with their brightness distribution, to double check the consistency of our results.

The maps are shown in Fig. C.5. The magnetic field topology of both stars does not change substantially. For StKM 1-1262, the poloidal energy fraction is increased by 3%, the dipolar by 6% (with consequent decrease in quadrupolar and octupolar fractions) and the axisymmetric component by 6%. The average field strength obtained when reconstructing Stokes I and V simultaneously is 15% lower. For V374 Peg, the configuration is more dipolar by 3% and axisymmetric by 6%, and the average field strength is 18% larger.

For the brightness map of StKM 1-1262, we observe a dark spot at a similar location than when reconstructing Stokes I alone, with a coverage slightly decreased to 8.5% and a lower contrast of 20% with respect to the quiet photosphere. In this case, the algorithm puts a bright feature at around phase 0.10 at a higher latitude with respect to the previous run with Stokes I alone, and shifts the phase of the already-present bright feature from 0.5 to 0.6. In the new reconstruction, the position of the bright features correlates with the location of the large-scale field component with negative polarity. For V374 Peg, the contrast of the brightness map is mostly dominated by a bright feature at around phase 0.4, which is the same pointing phase of the positive polarity of the large-scale magnetic field configuration. The code still reconstructs the same bright features at phases 0.2 and 0.6 and at a similar latitude, albeit with a smaller contrast with the quiet photosphere.

We note that magnetic effects can dominate the width of Stokes I LSD profiles rather than brightness inhomogeneities. Recent examples are the M dwarfs AU Mic and EV Lac described by Donati et al. (2023) and Donati et al. (2025), for which the authors find substantial differences in the width of Stokes I LSD profiles when computed with magnetically sensitive and insensitive lines separately. They assumed that the small-scale field locally scales up with the large-scale field, which allowed them to fit the Stokes I profiles width simultaneously with the Stokes V profiles, producing a large-scale magnetic field reconstruction consistent with the small-scale field. In our case, the change in width of the Stokes I LSD profiles is not large, likely due to rotational broadening being a dominant component, and its rotational modulation is not more or less evident when using magnetically insensitive and sensitive lines, respectively. Thus, we cannot apply the same methodology.

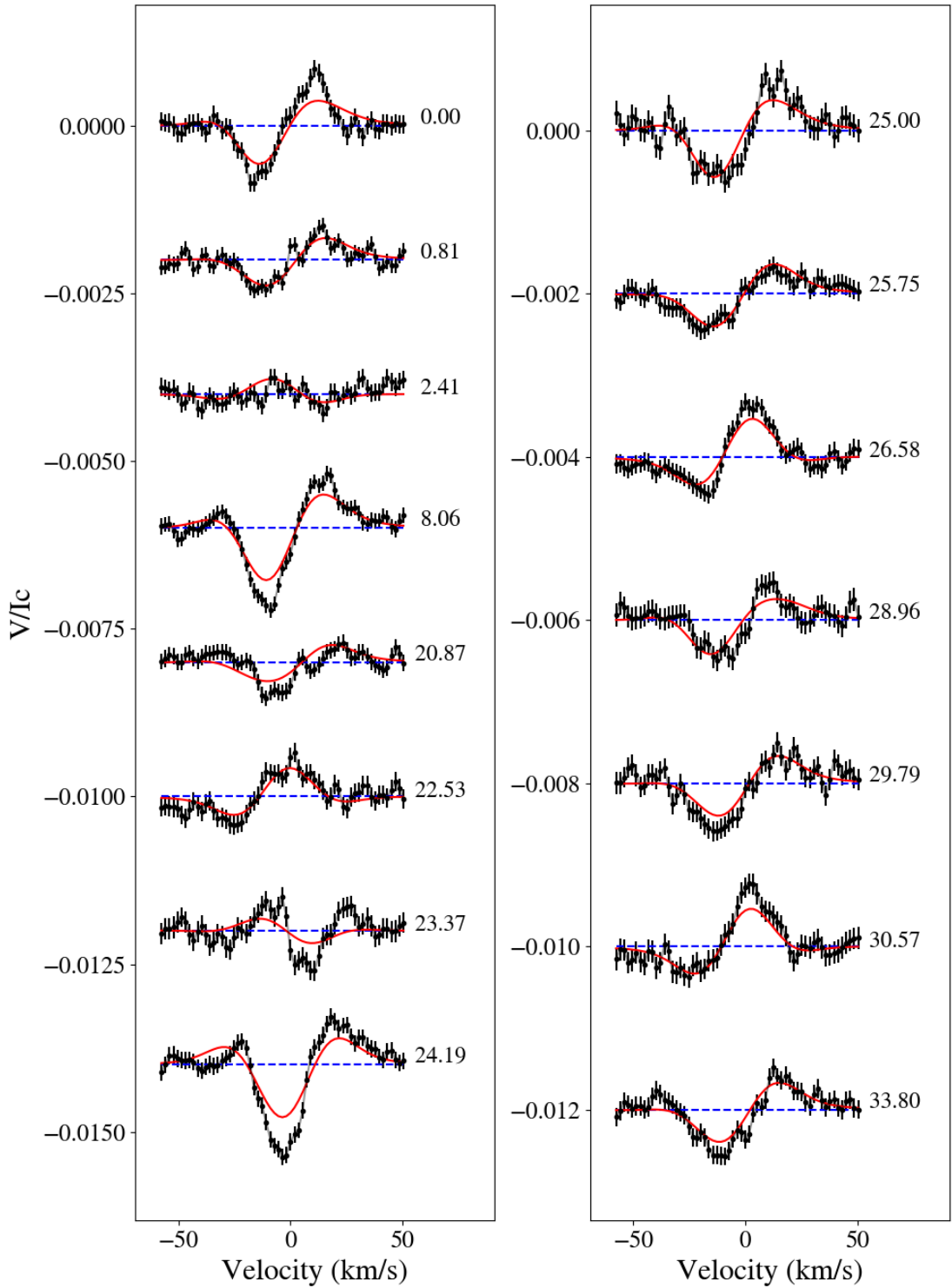


Fig. C.1. Time series of Stokes V LSD profiles and the ZDI models for StKM 1-1262. The observations are shown in black and the models in red. The numbers on the right indicate the rotational cycle computed from Eq. 1 using the first observation of an epoch as reference date. The horizontal line represents the zero point of the profiles, which are shifted vertically based on their rotational phase for visualisation purposes.

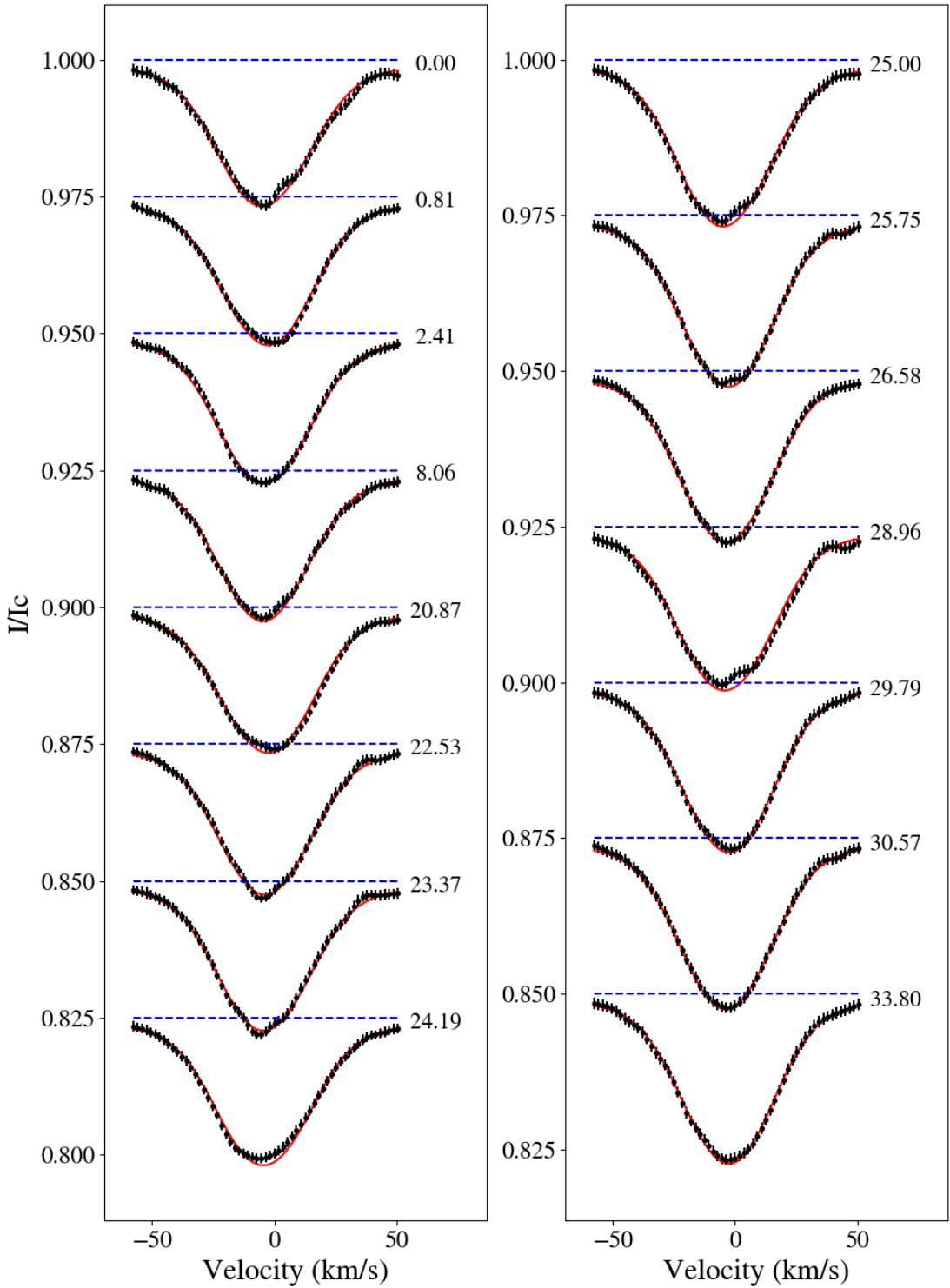


Fig. C.2. Time series of Stokes I LSD profiles and the DI models for StKM 1-1262. The format is the same as Fig C.1. The horizontal blue dashed line indicates the continuum level at 1.0, which is shifted vertically for visualisation purposes.

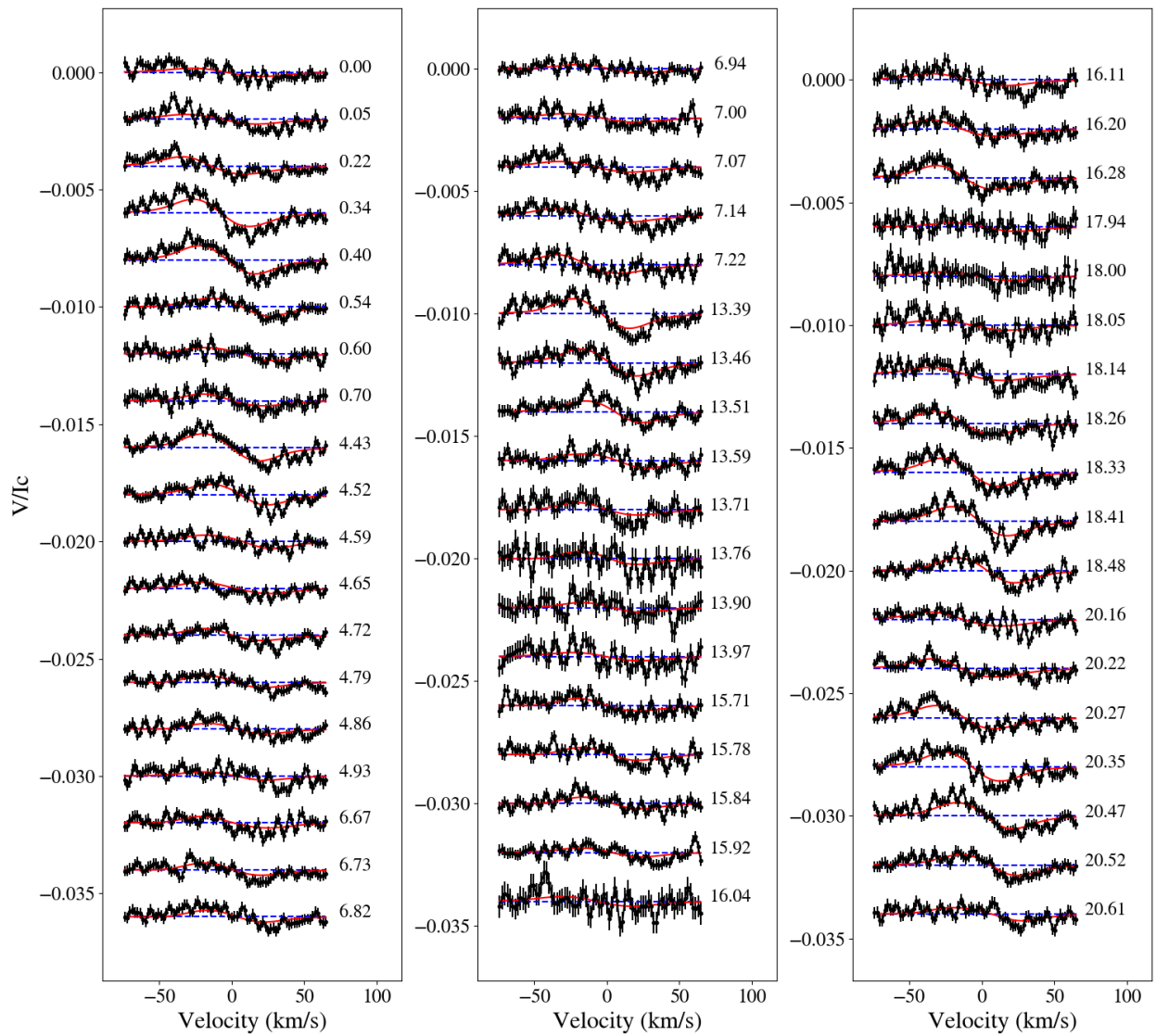


Fig. C.3. Time series of Stokes V LSD profiles and the ZDI models for V374 Peg. The format is the same as Fig. C.1.

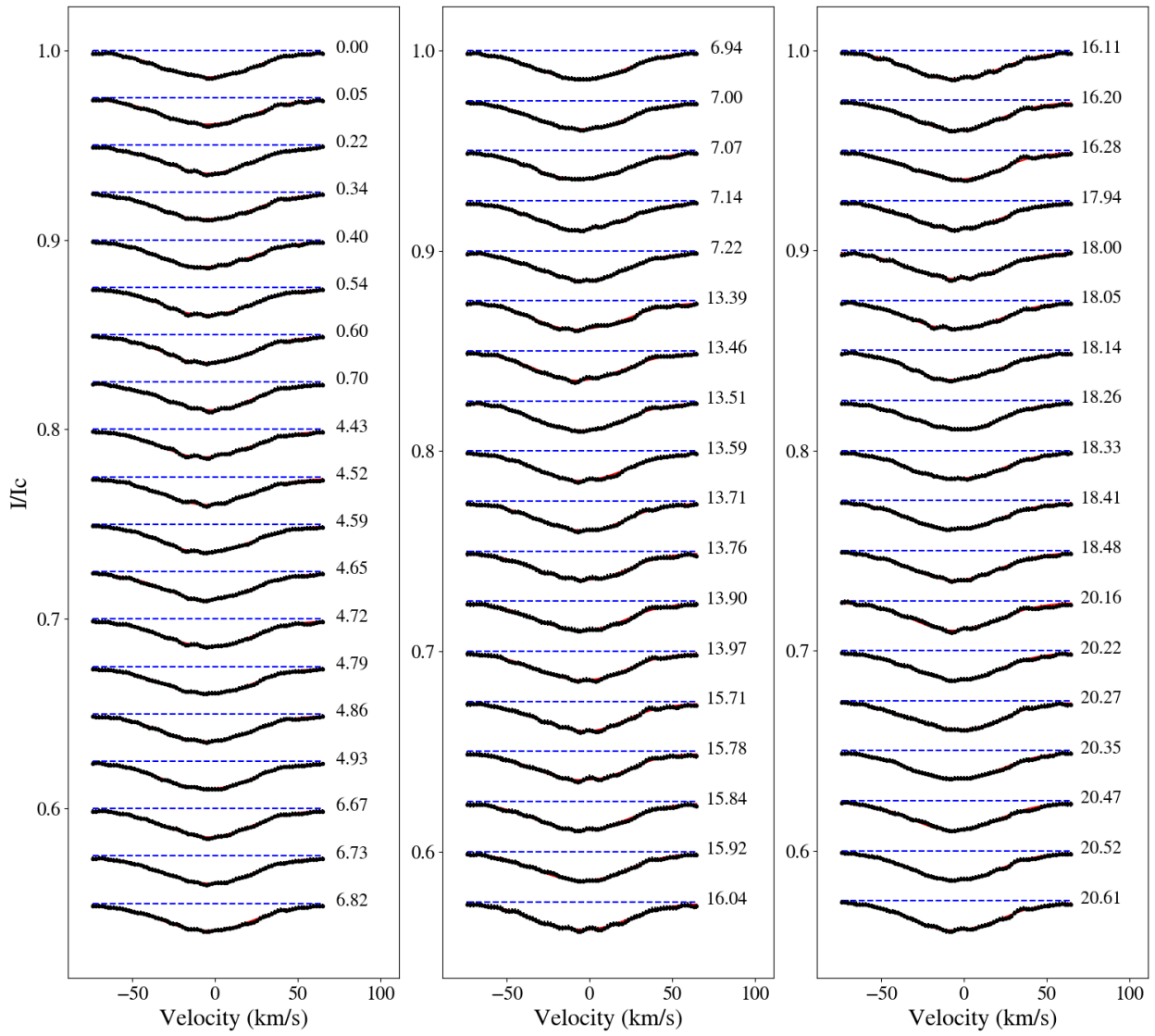
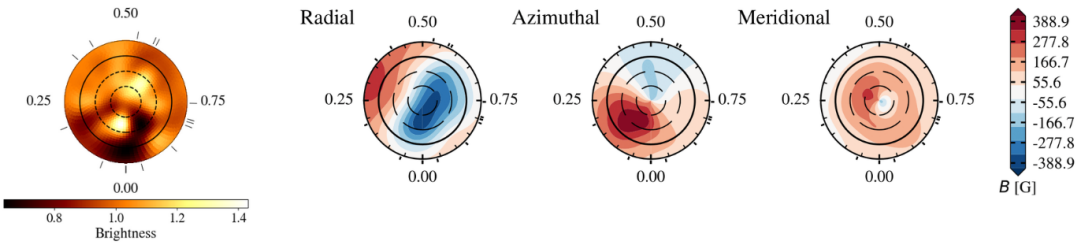


Fig. C.4. Time series of Stokes I LSD profiles and the DI models for V374 Peg. The format is the same as Fig. C.2.

StKM 1-1262



V374 Peg

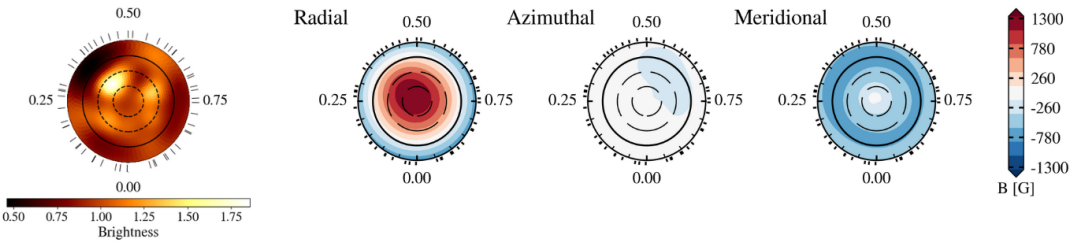


Fig. C.5. Simultaneous brightness and magnetic reconstruction. The format is the same as Fig. 7 for the brightness part and Fig. 5 for the magnetic part.